CrossMark

ROYAL
AERONAUTICAL
SOCIETY

REGULAR PAPER

Investigation of rarefied flow over an open cavity using direct simulation Monte Carlo

D. Nabapure* [iD], A. Singh [iD] and R.C.M. Kalluri

High-Performance Computing (HPC) Lab, Department of Mechanical Engineering, Birla Institute of Technology and Science-Pilani, Hyderabad, 500078, India
*Correspondence author. Email: p20150056@hyderabad.bits-pilani.ac.in

Abstract

The present study employs the direct simulation Monte Carlo (DSMC) technique to analyse the flow over a cavity, a commonly observed anomaly on a re-entry vehicle's surface. The flow characteristics are examined for different Mach numbers (Ma) and Knudsen number (Kn). The Mach numbers varied from 5 to 25, while the Knudsen numbers varied from 0.05 to 21.10. The influence of the Ma and Kn on flow characteristics has been elucidated graphically in various sections. The flow properties showed significant variation with Ma and Kn and showed an increasing trend due to compressibility and viscous heating effects. The surface characteristics were observed to diminish as Ma increases, while they showed complex trends for various Kn. In all flow regimes, there was an appearance of flow recirculation. When chemical reactions were taken into consideration and compared with non-reacting flows, flow temperature was primarily influenced (which decreased due to energy absorption) compared to other properties. The results obtained are a complex interplay of the viscous heating, compression and rarefaction effects.

Nomenclature

Abbreviations

BE	Boltzmann equation
DSMC	direct simulation Monte Carlo
MD	molecular dynamics
NSF	Navier-Stokes Fourier
PPC	particles per cell

Symbols

C_p	pressure coefficient
C_f	skin friction coefficient
C_h	heat transfer coefficient
d	molecular diameter [m]
f	distribution function
h	characteristic length-(Cavity height) [m]
H	channel height [m]
k_b	Boltzmann constant
Kn	Knudsen number
m	molecular mass [kg]
Ma	Mach number
n	number density [m^{-3}]

N	number of molecules
p	pressure [N/m^2]
q	heat flux [W/m^2]
R	gas constant [J/mol. K]
Re	Reynolds number
t	time [s]
T	temperature [K]
X	distance in x-direction [m]
Y	distance in y-direction [m]

Greek symbols

χ	mole fraction
ω	viscosity-temperature index
ρ	density of the gas [kg/m^3]
μ	viscosity of the gas [N.s/m^2]
τ	shear stress [N/m^2]
λ	mean free path [m]
ζ	degree of freedom
Δ	timestep
Θ	vibrational temperature
δ	boundary layer thickness

Subscripts

∞	free stream
w	wall
R	rotational
T	translational
V	vibrational
ov	overall

1.0 Introduction

Aerospace vehicles experience severe thermal and aerodynamic stresses while re-entry into the atmosphere, thereby demanding a careful construction of a thermal shield. It is generally desired to have a smooth shape of the re-entry vehicles. Still, discontinuities such as steps, gaps or cavities are often inevitable due to the placement of certain sensors, manufacturing tolerances, and the different expansion rates when dissimilar materials are adopted. Since these vehicles move at high velocities, often hypersonic, and encounter various regimes during their path, these surface discontinuities can be a prospective cause of high heat loads. These heat loads can create a sudden transition to turbulence and cause flow separation [1–5]. Thus, there is an inherent need to determine these loads for the vehicle to function safely [6, 7]. The estimation of these thermal and aerodynamic loads can be carried out by experimentation, which is a very costly affair. Numerical modeling and computations can be performed relatively easily and steadily, gaining significance [8–10].

Among the various surface discontinuities, the flow over a cavity is among the several forms of conceptual designs commonly seen in thermal protection systems of re-entry aerospace vehicles. The analysis of cavity flows offers a more in-depth perspective into the flow field and surface properties of those geometries similar in nature. The flow rarefaction is determined using the Knudsen number (Kn) [11, 12] given by,

$$\text{Kn} = \frac{\lambda}{h} \tag{1}$$

where λ depicts the mean free path, and h is the characteristic dimension under consideration.

The Knudsen number classifies the flow regimes as [13–15]: Kn $\leq$ 0.001 (Continuum regime), 0.001 $\leq$ Kn $\leq$ 0.1 (Slip regime), 0.1 $\leq$ Kn $\leq$ 10 (Transitional regime) and Kn $\geq$ 10 (Free-molecular

regime). The breakdown of continuum theory occurs as the flow approaches the slip regime owing to prevalent rarefaction results, thereby requiring the use of computational alternatives, such as molecular dynamics (MD), the solution of Boltzmann equations (BE), and direct simulation Monte Carlo (DSMC) [16].

The Kn, Re and Ma are related to each other by the relationship given by,

$$\text{Kn} = \sqrt{\frac{\pi \gamma}{2}} \frac{\text{Ma}}{\text{Re}} \text{ where Ma} = \frac{U_\infty}{\sqrt{\gamma RT}} \text{ also, Re} = \frac{\rho U_\infty h}{\mu} \tag{2}$$

where ρ denotes density, U_∞ free-stream velocity, h cavity depth and μ dynamic viscosity of the fluid.

Several studies featuring experimental, numerical and analytical are carried previously for analysing the flow characteristics [17–22] on surfaces of aerospace re-entry vehicles. However, in this introduction, we shall describe numerical studies that have been carried out in the past to study the flow field structure around cavities. Mankodi et al. [23] used the DSMC approach to investigate the flow field and surface properties over a stardust re-entry vehicle. Akhlaghi et al. [24] used the DSMC approach with a novel flow decomposition to investigate the rarefaction effects in a lid-driven cavity. Roohi et al. [25] also used the DSMC approach to investigate the cold to hot heat transfer and rarefaction effects in a nano-scale isosceles triangular cavity. Mohammadzadeh et al. [26] also performed a similar study for a micro-nano square cavity. Creighton and Hillier [27] carried out several studies on the hypersonic flow over annular cavities. They studied the consequence of cavity length to depth ratios on the flow field. Morgenstern and Chokani [28] used the CFD approach to investigate the unsteady hypersonic cavity flow and analysed the influence of Reynolds number and cavity length to height ratios (L/H) on the heat transfer rates. Palharini et al. [29] employed the DSMC approach to investigate the cavity flow and studied three-dimensionality's effect on the aerodynamic properties. Santos et al. [30] studied the impact of change in cavity height for a range of (L/H) ratio on the aerodynamic properties in a hypersonic cavity flow using DSMC. Guo et al. [31] applied the DSMC approach to numerically investigate the rarefied flow over various cavity shapes. They studied the effect of length-to-depth ratio, rear wall-to-front wall height ratio, and the inclination of the front wall and rear wall on the flow field properties. Guo et al. [32] also studied the 2-D hypersonic cavity flow for various Knudsen numbers ranging from continuum to transition regime and investigated the associated flow-field properties. Palharini et al. [33] employed the Quantum Kinetic (QE) modeling using the DSMC method to simulate chemical reactions for investigating the flow-field structure characteristics in a 3-D hypersonic flow over a cavity for several length-to-depth (L/D) (length to depth) ratios. In another study, Palharnini et al. [34] applied the DSMC method and conducted a thorough analysis on the effect of change in cavity length for different (L/D) ratios of the cavity in the transitional regime. Jin et al. [35] using the DSMC approach studied the impact of the Maxwellian accommodation coefficient on the rarefied hypersonic flows over 3-D cavity flows in the transitional regime.

From the literature study, it is observed that the majority of the studies employ the DSMC method due to its capability of modeling flows involving various rarefaction regimes. Nonetheless, the aerothermodynamic conditions encountered by hypersonic re-entry vehicles are challenging to analyse owing to the multiple complexities involved. Therefore, the physical dynamics of such extremely rarefied hypersonic flows are not adequately recorded in the open literature. Also, a significant chunk of the work focuses on studying the effects of cavity geometry, primarily in the transitional regime. Minimal studies have been carried out on cavity flows in the other regimes, particularly the free molecular regime. This paper aims to bridge the gap and explores the flow-field and aerodynamic properties for non-reacting hypersonic cavity flow. The study mainly focuses on examining the influence of the Mach number and Knudsen number on the flow field and aerodynamic characteristics.

This study is structured into the following sections: Section 2 summarises the computational technique employed. Section 3 summarises the validation and verification studies carried out. Section 4 thoroughly illustrates the Mach number and Knudsen number effects on the flow field and surface properties. Also, a comparison is made with chemically reacting flows to explain the differences observed. Finally, Section 5 lists critical conclusions from the study.

2.0 Methodology

In this section, a brief description of the computational approach employed for the analysis, the problem statement, and the various computational parameters used in the investigation are provided.

2.1 Direct simulation Monte Carlo

Pioneered by Bird [36] in the early 1960s, the DSMC method is one of the most popular and successful techniques to analyse rarefied gas flows. The DSMC method is a probabilistic method for modeling gas flows in a rarefied regime [37]. This technique involves simulated particles, each representing a substantial number of actual molecules. The motion of particles and their collision interactions describe the physics of gas. The transportation of mass, momentum and energy at the microscopic size is assessed. Movements are modeled in a deterministic way, whereas the collisions in a stochastic manner. The separation of the deterministic molecular movements and the stochastic inter-molecular collisions form the central hypothesis of the DSMC technique. The particle data averaged over a considerable number of time steps; mostly millions give the macroscopic properties. Despite the development of other methods, the DSMC plays an important role in solving rarefied gas dynamics problems. It addresses many issues, including high-altitude aerodynamics, plume impingement, laser ablation and rarefied plasma [38–40]. The technique can also be implemented to the continuum regime; however, it is computationally costly [41].

As known, the air density declines steadily as the elevation rises, and the effects of rarefaction effects are more prevalent. Also, the flow enters the free-molecular regime, the breakdown of Navier Stokes Fourier (NSF) equations takes place [13], paving the way to use the Boltzmann equation [42]. The Boltzmann equation is not handled directly by the DSMC technique; instead, it is a mere simulation technique that models the flow physics. The Boltzmann equation [43] is given by,

$$\frac{\partial f}{\partial t} + \boldsymbol{v}.\nabla_x f = \frac{1}{\text{Kn}} Q(f,f) \ , \ \ \boldsymbol{x}\varepsilon\mathbb{R}^{dx} \ , \ \boldsymbol{v}\varepsilon\mathbb{R}^{dv} \tag{3}$$

Where $f(t, x, v)$ represents the density distribution function at a location $\boldsymbol{x}$, velocity $\boldsymbol{v}$ and at time t. Kn signifies the Knudsen number and the collision operator $Q(f,f)$ indicates the binary collisions that occur.

The DSMC process involves calculation at every time step the movement and intermolecular collision of a finite number of fictitious particles separately, considering that each particle constitutes a considerable number of actual particles. The physical space under investigation is represented by a computational grid, divided into many cells for selecting collision pairs. The cell sizes should be kept of the order of or smaller than the local mean free path [44]. Also, the timestep used should be smaller than the mean collision time [45]. The DSMC technique is susceptible to many statistical errors as it is probabilistic centred and relies on multiple thousands or millions of simulated molecules. Quantitative research showed that such errors were inversely proportional to the sample size square root. Thus, a condition of a minimum number of DSMC particles per cell (PPC) should be satisfied. Therefore, to decrease this significant error, an exact DSMC simulation should involve an appropriate number of particles in a cell, generally 15–20. However, this brings its own computational challenges. Therefore, it is necessary to determine the optimum number of particles in each cell so that statistical accuracy, along with a realistic computational expenditure, can be maintained.

There are many schemes to select a collision pair; a review is given in Refs. (46 and 47). Here, the No Time Counter scheme (NTC) [48] is employed. The DSMC also involves numerous collision models explained in Ref. (49); among them, the Variable Hard Sphere (VHS) collision model is adopted here.

In this study, DSMC computations employed the *dsmcFoam* code [50, 51]. The code is highly efficient and scalable by adapting efficient parallelisation techniques such as OpenMPI. The code has been validated on various problems in rarefied gas flows.
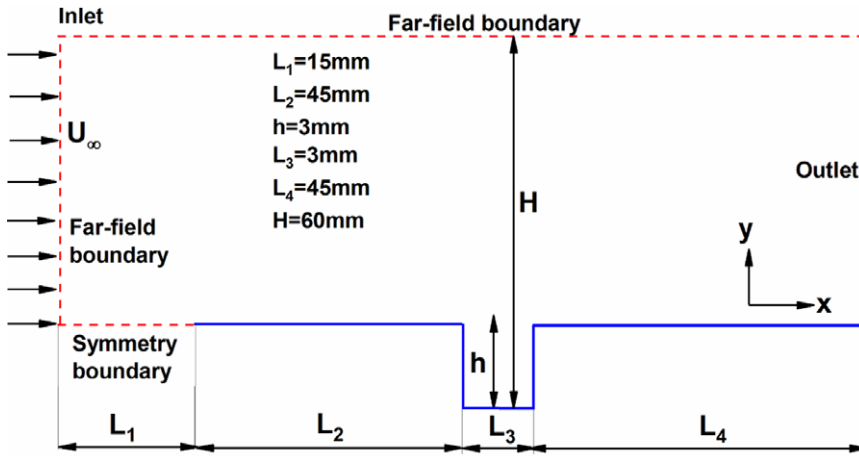
Figure 1. *Schematic illustration of the 2-D cavity problem.*

2.2 Problem statement

The schematic illustration of the 2D cavity is shown in Fig. 1. The fluid movement occurs from left to right. The flow along the streamwise and transverse directions is depicted by the coordinates *x* and *y*. The length and depth of the cavity were fixed to 3mm. The domain height at the outlet was set at H = 60mm after conducting an influence study on the flow properties.

2.3 Boundary conditions and computational grid

The different boundary conditions applied on the surfaces and dimensions of all the parameters are as shown in the computational domain in Fig. 1. The left and top boundaries represent the far-field boundary condition through which the simulated particles enter and leave the domain. The right boundary denotes the outlet, where the particles exit [52, 53]. The solid boundary (blue) represents the open cavity and is given a diffused reflection with full thermal accommodation condition. In a diffuse reflection model, the simulated molecules are equally reflected in all directions. The initial length of 15mm from the inlet to the edge of the cavity represents symmetry and is used to accomplish a precise velocity in the perpendicular directions [46]. Thus, this surface is analogous to a specular reflecting model.

The computational domain is divided into several blocks and meshed in a structured manner, as shown in Fig. 2. The cell widths in both *X* and *Y* directions were maintained below the mean free path, i.e. Δx_{cell}, $\Delta y_{cell} < 0.3\lambda_{\infty}$. The cell size was refined near the cavity. The total number of cells for the case of Kn = 1.06 was about 40,548 cells. Also, the cell count varied for other cases depending on the corresponding mean free path.

Tables 1 and 2 show the gas properties and the free-stream flow parameters employed in the present simulations. Such flow characteristics are experienced by a hypersonic vehicle during its re-entry and are taken from the U.S. Standard Atmosphere charts [54]. The fluid considered is non-reacting air having a molecular weight of about 28.96g/mol with a major composition of 76% N_2 and 23% O_2. The inflow Mach number considered was Ma = 25 and it was constant for all cases. Also, all the wall surface (T_w) was maintained at four times the free-stream temperature $4T_{\infty}$. In the initial studies, the simulations were conducted considering air as non-reacting rarefied perfect-gas and the chemical reactions were relaxed. This assumption has been used in numerous published studies [29, 34, 35, 55]. In Table 3, χ denotes the mole fraction, *m* denotes the molecular mass, *d* the molecular diameter ω represents temperature dependent viscosity index and ζ represents the degrees of freedom.
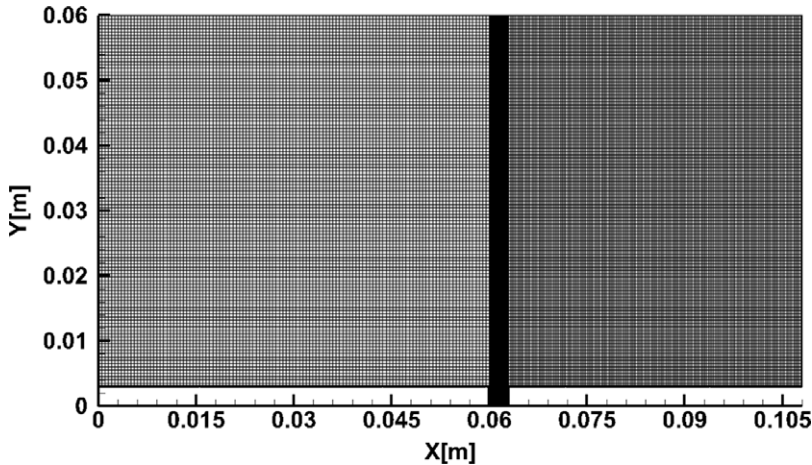
Figure 2. *The meshed domain.*

Table 2 lists the inflow boundary conditions, which show the different atmospheric altitudes examined, ranging from 55 to 95Km. All the simulations ran for about 1.5ms of flow time, which consisted of 75,000 timesteps and employed about 276,500 simulated particles. The time averaging of the DSMC particle fields was started once the total DSMC particles reached a steady state. The solution was considered steady-state when the average linear kinetic energy of the system showed no significant variation [50]. The Knudsen number (Kn_h) and Reynolds number (Re_h) were estimated by choosing the cavity depth (h) as the characteristic dimension.

3.0 Model validation

In the section, the validation studies performed to assess the accuracy of the solver are explained. Firstly, without considering the chemical reactions, the validation was carried for flow over a cavity. Then, the solver was validated, accounting for the chemical reactions using a cylinder test case.

3.1 Flow over cavity

The analyses in this paper are carried out using the *dsmcFoam* solver. The solver has been examined in different cases [56–66] in our previous studies. For a comparable case of flow over the cavity, the validation studies were carried out, and the results were compared against that of Guo et al. [31]. Guo et al. studied the flow over a cavity in different regimes for different L/D ratios of the cavity. *L* denotes the cavity length, and *D* represents the cavity depth, respectively. The flow conditions of the case are shown in Table 3.

For visual validation, the Mach number contours, and the streamlines are compared. The simulated results are reasonably similar to the published results of Guo et al., as observed in Fig. 3. Furthermore, the Mach number and temperature profile along the surface at a depth $D = 0.5$ for an $L/D = 5$ is shown in Fig. 4(a) and (b). Comparing the simulated results with Guo et al. reveal no significant deviation in the profiles depicting close alignment between present DSMC computations and the other literature findings.

3.2 Flow over cylinder

To validate the solver with incorporating the chemical reactions, a test case of the cylinder was simulated. A 2-D hypersonic rarefied air flow over a circular cylinder with a diameter of 2m, examined by

Table 1. *Properties of the gas* [55]

	χ	m, kg	d, m	ω	ζ
O_2	0.237	5.312×10^{-26}	4.07×10^{-10}	0.77	5
N_2	0.763	4.650×10^{-26}	4.17×10^{-10}	0.74	5

Table 2. *Inflow boundary conditions* [54]

| Altitude	55.02km	60.5km	77km	91.5km	95km
Free-stream velocity (U_∞) [m/s]	8050.75	7829.25	7134.5	6851.38	6887.03
Inlet gas temperature, (T_∞) [K]	259.39	245.64	204.49	186.89	188.84
Wall temperature, (T_w) [K]	1037.56	982.56	817.96	747.56	755.36
Free-stream pressure, (p_∞)[N/m^2]	39.86	20.51	1.72	0.14	0.069
Mass density, (ρ) [kg/m^3]	5.35×10^{-4}	2.90×10^{-4}	2.94×10^{-5}	2.61×10^{-6}	1.27×10^{-6}
Number density, (n_∞) [m^{-3}]	1.11×10^{22}	5.62×10^{21}	5.29×10^{20}	5.45×10^{19}	2.66×10^{19}
Mean free path, (λ_∞) [m]	1.51×10^{-4}	3×10^{-4}	3.19×10^{-3}	3.1×10^{-2}	6.33×10^{-2}
Reynolds number (Re_h)	783.11	431.10	46.61	4.29	2.08
Knudsen number (Kn_h)	0.05	0.10	1.06	10.33	21.10

Table 3. *Computational details of Guo et al.* [31]

T_∞ (K)	p_∞ (N/m^2)	Ma	ρ_∞ (kg/m^3)	λ_∞ (m)	Kn
219.59	5.221	10	8.28×10^{-5}	9.81×10^{-4}	0.327
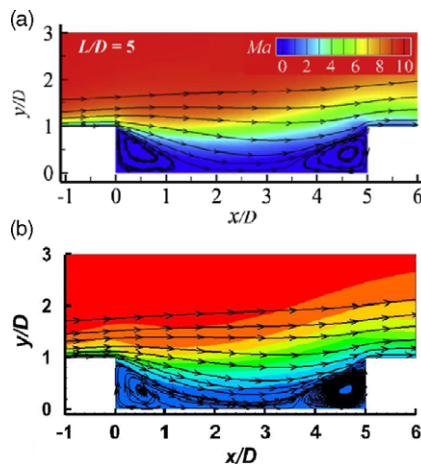
Figure 3. *Distribution of Mach number contours and streamlines for cavities with $L/D = 5$. (a) Published results* [31] *(b) Present study.*
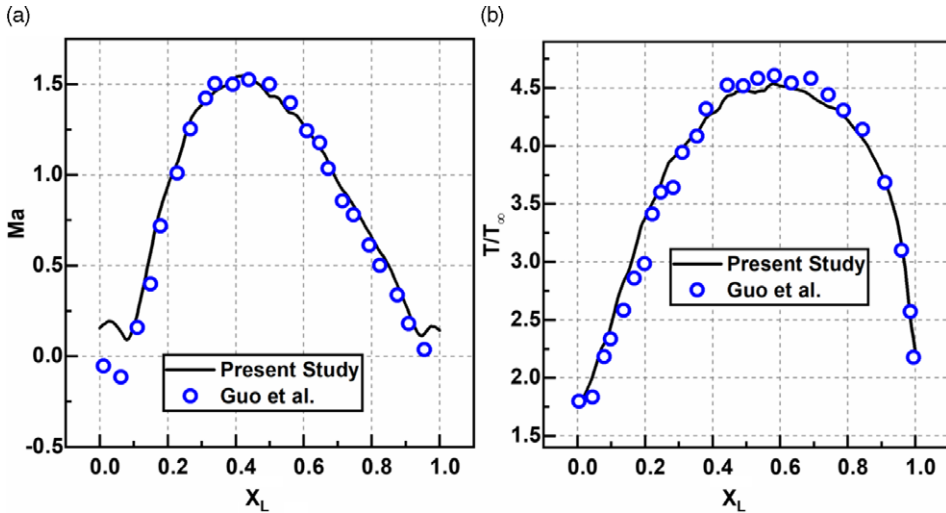
Figure 4. *Comparison of (a) Mach number and (b) temperature ratio profiles for the depth of 0.5D.*

Scanlon et al. [67], was used as a standard case, and the Quantum-Kinetics (Q-K) chemical reaction model was considered. The computational conditions considered for the case are given in Table 4. The cylinder was maintained at a temperature of 1000K, and the cylinder walls are fully diffuse with full thermal and momentum accommodation coefficients. This study was carried out using *dsmcFoam+*. Figure 5(a) shows the comparison of contours of Mach number between Scanlon et al. and the current simulation. From the contours, a reasonable agreement among them is observed. The number density of the species along the stagnation line of the cylinder is shown in Fig. 5(b), which shows a good overlap. Thus, the findings are consistent with those reported by Scanlon et al., establishing the validity of our outcomes.

4.0 Results and discussion

In the analysis of re-entry vehicles, the flow field and the aerodynamic surface properties play a crucial role. Hence in this section, the influence of the free-stream Mach number and the Knudsen number's influence is thoroughly investigated. The flow properties such as velocity, pressure, temperature and surface properties such as pressure coefficient, skin friction coefficient and heat transfer coefficient are presented in detail.

Prior to discussing the flow field and aerodynamic properties, the contours are presented in brief. For the case of Ma = 25, Kn = 1.06, the various flow-field contours are shown in Fig. 6. Figure 6(a) shows the non-dimensional velocity contour that depicts the hydrodynamic boundary layer's growth, with lower magnitudes at the wall and higher magnitudes away from it in the central domain. Downstream of the step, the velocity magnitudes are very low due to flow recirculation. Also, the band of near-wall low velocity extends from the step to the outlet region.

The non-dimensional density contour shown in Fig. 6(b) shows a higher density near the upstream wall and a gradual reduction away from it. The density magnitude is close to one in the majority of the computational domain. The region close to the step has low-density magnitudes due to the recirculation and expansion effects. Furthermore, a high-density magnitude band arises from the upstream surface and traverses towards the top surface, causing a regionalised density rise.

The non-dimensional pressure contour is shown in Fig. 6(c), which attain greater values at the upstream wall and are one order greater than that of free-stream. Due to the minimal influence of the step in the central domain, pressure attains the free-stream value. In the downstream direction, the pressure

Table 4. *Computational details of Scanlon et al. [67]*

H	T_∞	Ma_∞	Cylinder diameter	Mean free path	Collision frequency	Inflow density
(Km)	(K)	–	(m)	(m)	(1/s)	(kg/m^3)
86	187	25	2	1.23×10^{-2}	2.96×10^4	1.43×10^{-5}
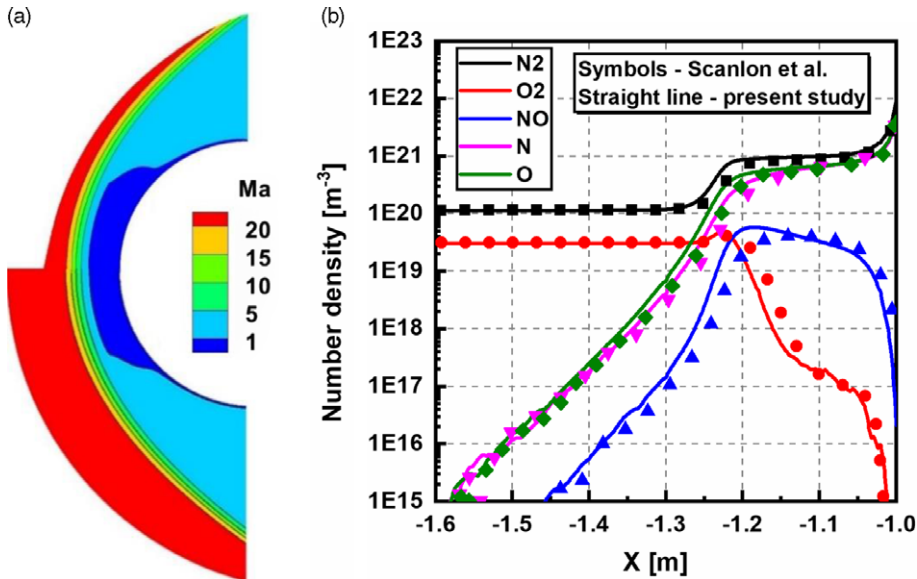
Figure 5. *(a) Mach number contour reported by Scanlon et al. [67] (lower half) and current simulation results (upper half), (b) Number density along the stagnation line.*

magnitudes are very low due to the recirculation. Also, the wall pressures are lower than their upstream counterparts, primarily due to the flow expansion.

The non-dimensional temperature contour is shown in Fig. 6(d), which follows the pressure contour and depicts higher magnitudes near the wall due to the viscous heating and compressibility phenomena. The band of high temperature at the step height level continues to dissipate the energy farther downstream of the step. Similar to the pressure contour, the non-dimensional temperature also shows lower magnitudes close to the step; however, these low temperatures are confined to a lower region than the pressure.

The compressibility (Z) contour is shown in Fig. 7. The compressibility factor shows the departure of the gas from the ideal behaviour and is given by

$$Z = \frac{p}{\rho R T} \tag{4}$$

where p denotes the pressure, ρ the density, R the gas constant, and T is the temperature.

The regions of higher Z magnitudes are witnessed on the upstream surface due to the shear effects. A similar trend is noticed downstream of the step; however, the magnitudes of Z are lower compared to the upstream. Inside the cavity, the magnitudes of Z are relatively low, depicting equilibrium.

4.1 Influence of Mach number

In this section, the influence of Mach number (Ma) is presented. The various Ma considered for analysis were 5, 10, 25, and 30. The Knudsen number and wall temperature was fixed to Kn = 1.06 and
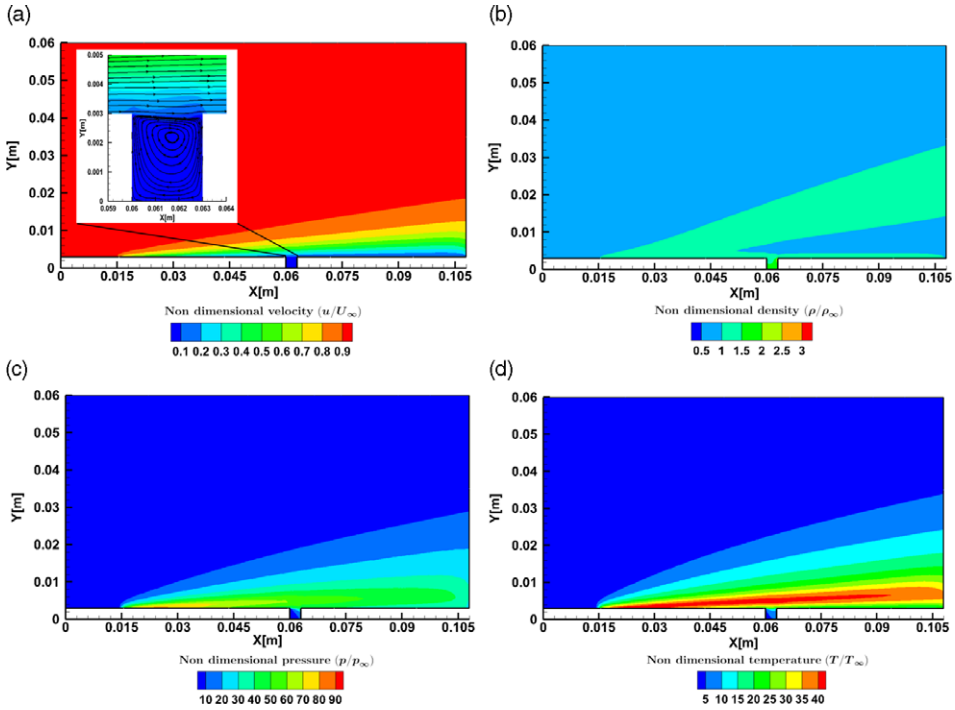
Figure 6. *Contours of non-dimensional (a) velocity, (b) density, (c) pressure, and (d) temperature for* $\mathrm{Ma} = 25$ *and* $\mathrm{Kn} = 1.06$.
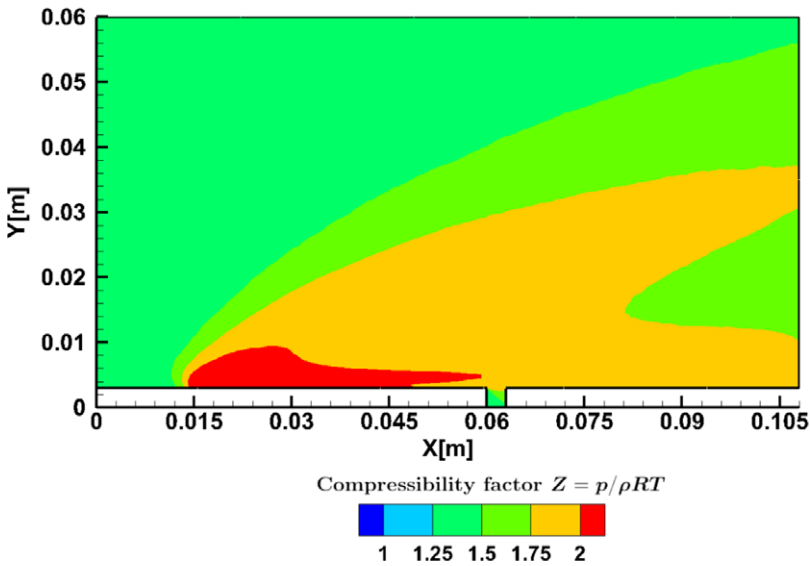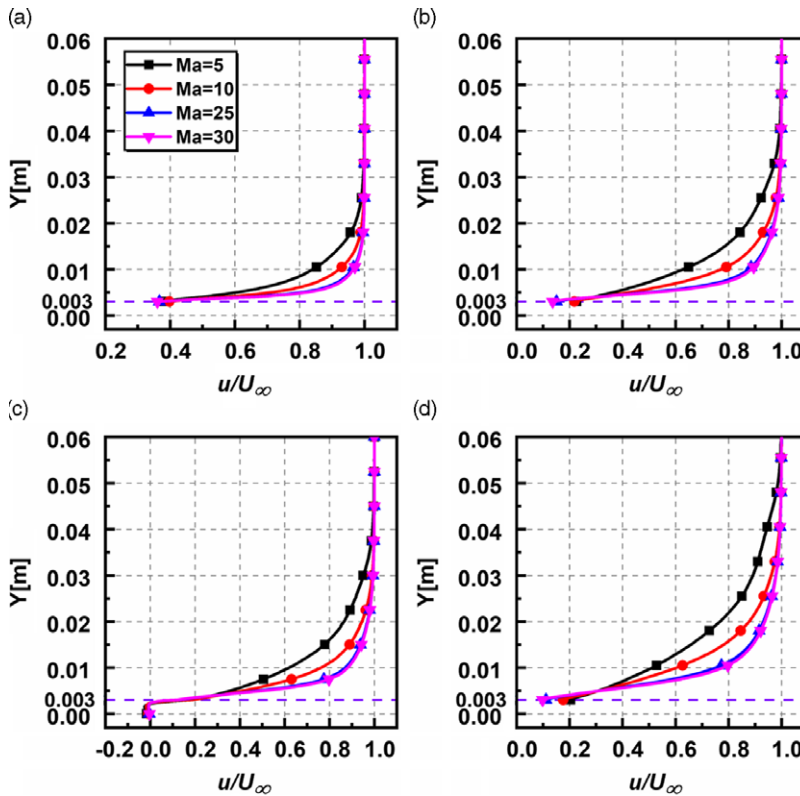

**Figure 7.** *Compressibility (Z) contour for* $\mathrm{Ma} = 25$ *and* $\mathrm{Kn} = 1.06$.

Figure 8. *Non-dimensional velocity variation for various* Ma *at (a)* $X = 30$mm, *(b)* $X = 59$mm, *(c)* $X = 61$mm, *(d)* $X = 93$mm.

$T_w = 4T_\infty$ respectively. Along the transverse direction, the properties are evaluated at four different X locations, namely $X = 30$, 59, 64 and 93mm, respectively. (The dashed purple line in the following figures represents the level of the cavity height $h = 0.003$m.)

4.1.1 Flow properties

a) Velocity field. The non-dimensional velocity (u/U_∞) variation for various Ma at sections $X = 30$mm, $X = 59$mm, $X = 61$mm and $X = 93$mm is shown in Fig. 8(a–d). Y denotes the perpendicular distance in y-direction above the cavity surface. The non-dimensional velocity at $X = 30$mm and $X = 59$mm are found to be overlapping for different Ma away from the wall, depicting the flow is not influenced due to the presence of the cavity. Inside the cavity for $X = 61$mm, the non-dimensional velocities are negative, portraying flow recirculation. This observation aligns with the continuum results of Grotowsky and Ballmann [68] and that of Camussi et al. [69] for comparative geometries. Also, the plots overlap for different Ma up to the height of the cavity and deviate after that, signifying that the change in Ma has relatively less influence on the velocity field inside the cavity. At section $X = 93$mm, away from the bottom surface, the variation is similar to the one found on the upstream side. Near-wall slip is observed at all the sections except inside the cavity where the recirculation takes place. Furthermore, the boundary layer thickness decreases with an increase in Ma as observed for continuum flows.

b) Pressure field. The non-dimensional pressure (p/p_∞) variation for various Ma at sections $X = 30$mm, $X = 59$mm, $X = 61$mm and $X = 93$mm is shown in Fig. 9(a–d). Near the inlet of the domain at $X = 30$mm, the pressure magnitudes are higher and are two orders greater than the free-stream pressure. At $X = 59$mm, the pressure magnitudes are less and show deviation for different Ma. Inside the
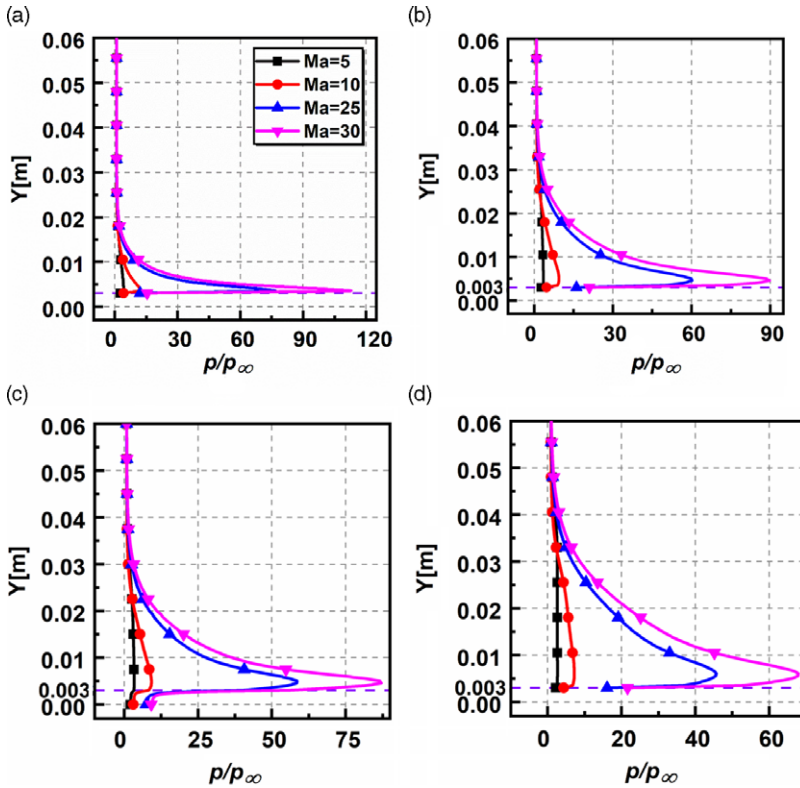
Figure 9. *Non-dimensional pressure variation for various* Ma *at (a)* $X = 30$mm, *(b)* $X = 59$mm, *(c)* $X = 61$mm, *(d)* $X = 93$mm.

cavity at $X = 61$mm, the pressure magnitudes are lower due to the recirculation and expansion effects. Below the cavity depth (for $Y < 0.003$), the pressure reduces and attains the free-stream magnitudes, whereas, above the cavity (for $Y > 0.003$), the pressure magnitudes reach a peak shortly, after that the profiles overlap near the centre of the domain. For reference, at section $X = 61$mm, the peak pressure ratios are 3.41, 9.22, 58.57 and 87.03 for Mach numbers 5, 10, 25 and 30. Also, for different Ma, the near-wall pressure is relatively similar when compared to the other sections. The pressure magnitudes are lower downstream of the cavity and show distinct variation for different Ma and attain free-stream magnitudes at a more considerable distance in the transverse direction. Thus, the non-dimensional pressure magnitudes are directly influenced by the Ma and increase with increasing Ma due to viscous heating.

c) Temperature field.   The non-dimensional temperature (T/T_∞) variation for different Ma at sections $X = 30$mm, $X = 59$mm, $X = 61$mm and $X = 93$mm is shown in Fig. 10(a–d). In $X = 30$mm, the temperatures near the wall are of higher magnitudes than the imposed wall temperature owing to viscous heating effects and soon overlap in the transverse direction. The profiles in section $X = 59$mm are similar but take a longer distance in the transverse direction to coincide and attain temperature close to the free-stream magnitude. Inside the cavity at $X = 61$mm, identical to the pressure, the near-wall temperatures for different Ma seem to be unaffected and are found to be relatively the same. This is due to the recirculation region, which causes the flow to stagnate and reduces the temperatures. For quantitative assessment at section $X = 61$mm, on the top face of the cavity, the peak temperature ratios are 4.39, 8.70, 42.50 and 60.44 for Mach numbers 5, 10, 25 and 30. Near the exit of the domain at $X = 93$mm, the plots are similar but of a marginally lower magnitude. At the same level as the cavity entrance, the
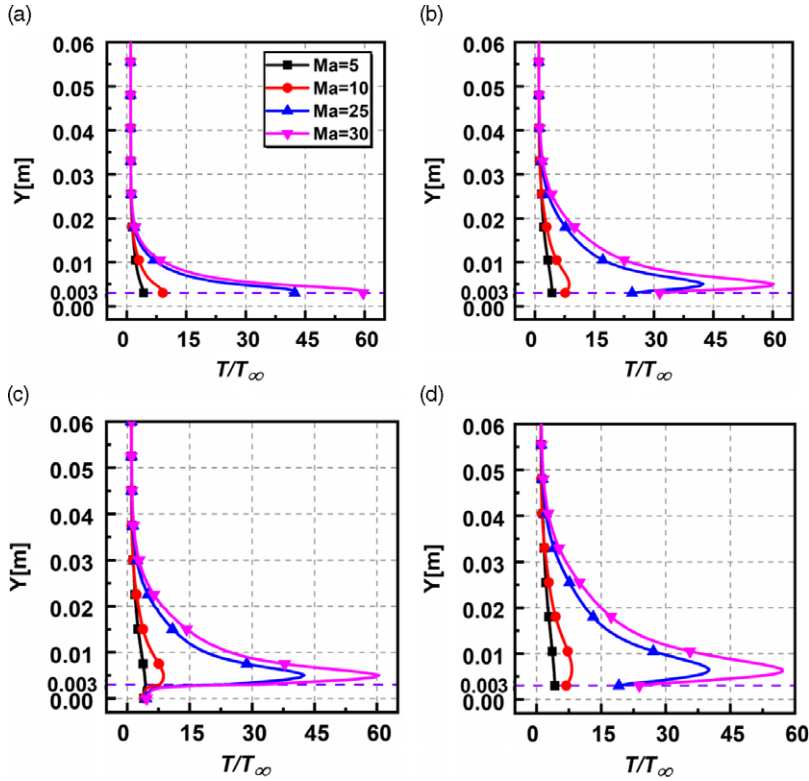
Figure 10. *Non-dimensional temperature variation for various* Ma *(a)* $X = 30$mm, *(b)* $X = 59$mm, *(c)* $X = 61$mm, *(d)* $X = 93$mm.

peak magnitudes of temperatures are observed in the shear layer. Thus, it is observed that similar to the pressure; the temperatures are directly influenced by the change in Ma and show an increasing trend.

4.1.2 Aerodynamic surface properties

a) Pressure coefficient.   The variation of pressure coefficient (C_p) for different Ma on the upstream, downstream, and the base surface of the cavity is shown in Fig. 11(a–b), C_p is given by

$$C_p = \frac{p_w - p_\infty}{\frac{1}{2}\rho_\infty U_\infty^2} \tag{5}$$

where, p_w denotes pressure at the wall, U_∞ is the free-stream velocity, p_∞ the free-stream pressure and ρ_∞ the free-stream density, respectively. Equation (6) shows that the pressure at the wall is extracted by computing the summation of momentum fluxes in the perpendicular direction for the incident and reflected molecules at every time step.

$$p_w = p_{inc} - p_{ref} = \frac{F_N}{A\Delta t} \sum_{j=1}^{N} \left\{ \left[(mv)_j\right]_{inc} - \left[(mv)_j\right]_{ref} \right\} \tag{6}$$

where, F_N signifies the amount of real particles that are characterised by each simulated particle, A denotes the surface area, Δt denotes the time step, m represents the mass of the particles, N indicates the number of particles colliding with surface per unit time per unit area and v denotes perpendicular component velocity of particle j. Subscripts *inc* and *ref* signify the incident and reflected molecules, respectively.
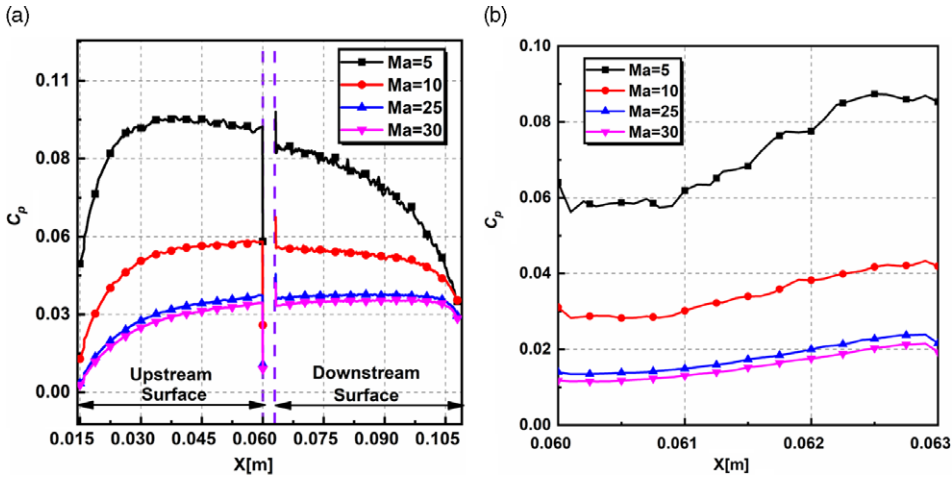
Figure 11. *Variation of pressure coefficient C_p (a) on the upstream and downstream surfaces (b) on the cavity base for various* Ma.

Figure 11(a) shows that the pressure coefficient C_p is found to behave in a similar manner for different Ma, showing a nonlinear trend, resembling a parabolic profile. Along the upstream surface, the magnitude of C_p gradually increases from the inlet. At the edge of the cavity the C_p reduces significantly. This can be attributed to the flow being expanded due to the increased area. Along the beginning of the downstream surface, stagnation pressure causes a surge in magnitudes of C_p. Subsequently the C_p shows a reducing trend towards the outlet. At the outlet, the magnitudes of C_p are greater than zero showing that the wall pressure is greater than the free-stream pressure. Inside the cavity, as shown in Fig. 11(b), the pressure coefficient C_p has a significantly lower magnitude due to the flow recirculation which causes a reduction in pressure. Along the cavity the C_p gradually increases for the lowest case of Ma = 5, whereas it is reasonably constant for the other cases. Thus, to summarise, the increase in Ma causes a reduction in C_p. As the Mach number increases the free-stream velocity increases and the contribution of the inertial term $\frac{1}{2}\rho_\infty U_\infty{}^2$ in the Equation (5) which causes a reduction in the magnitude of pressure coefficient.

b) Skin friction coefficient.   The skin friction coefficient (C_f) variation for different Ma on the upstream, downstream and the base surface of the cavity is shown in Fig. 12(a–b). C_f is given by

$$C_f = \frac{\tau_w}{\frac{1}{2}\rho_\infty U_\infty{}^2} \tag{7}$$

where, τ_w denotes the shear stress at the wall, U_∞ is the free-stream velocity, and ρ_∞ the free-stream density. The shear stress at the wall is extracted by computing the summation of the tangential momentum fluxes of the incident and reflected molecules at every time step and is given by,

$$\tau_w = \tau_{inc} - \tau_{ref} = \frac{F_N}{A\Delta t}\sum_{j=1}^{N}\left\{\left[(mu)_j\right]_{inc} - \left[(mu)_j\right]_{ref}\right\} \tag{8}$$

where u is the tangential component of the velocity of particle j.

In the present study, the walls are modeled using diffuse reflection gas-surface interaction; hence the tangential momentum of the reflected molecules is zero. Therefore, Equation (8) reduces to

$$\tau_w = \tau_{inc} = \frac{F_N}{A\Delta t}\sum_{j=1}^{N}\left\{\left[(mu)_j\right]_{inc}\right\} \tag{9}$$

Figure 12(a) shows that the skin friction coefficient C_f which follows the pressure coefficient and behaves similarly for different Ma. Along the upstream surface, the magnitude of C_f is greater at the beginning
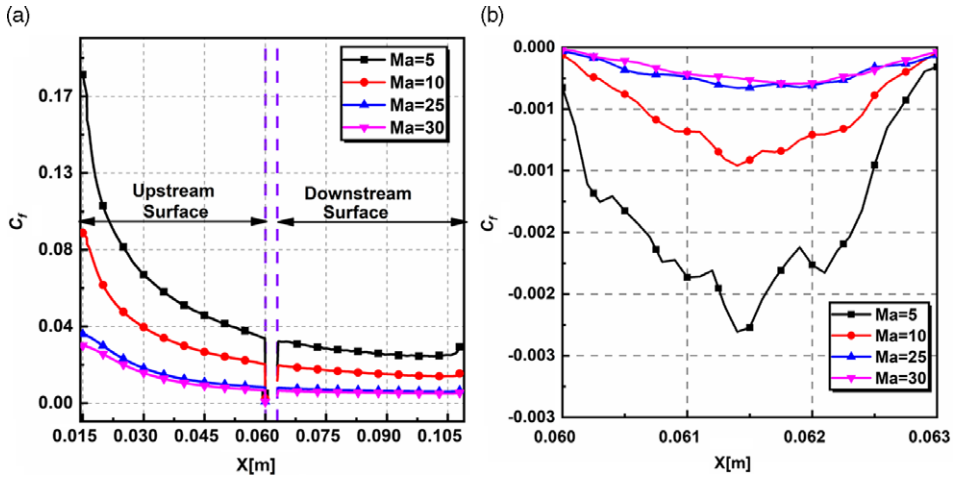
Figure 12. *Variation of skin friction coefficient C_f (a) on the upstream and downstream surfaces (b) on the cavity base for various* Ma.

due to the high-velocity gradients at the wall. This also causes the peak magnitudes of C_f near the upstream edge. From the upstream edge, C_f gradually decreases along X. Near the edge of the cavity C_f reduces significantly. Along the downstream surface, the magnitude of C_f surges quickly at a very short distance from the cavity and remains almost a constant towards the outlet. At the outlet, the magnitudes of C_f are again greater than zero, as observed in the pressure coefficient. Inside the cavity, C_f is found to be negative for all the cases due to the formation of recirculation region. The reduction in the magnitude is highest for the case of lowest Ma $= 5$. Thus, similar to the pressure coefficient C_p, the increase in Ma causes a reduction in C_f. This trend can be explained using the relation, $\mathrm{Kn} = \sqrt{\frac{\pi\gamma}{2}\frac{\mathrm{Ma}}{\mathrm{Re}}}$. For a given Knudsen number, the Mach number is proportional to the Reynolds number. Thus, as the Mach number increases, it causes an increase of the Reynolds number, leading to the domination of the inertial term in Equation (7). Thus, the magnitude of skin friction coefficient reduces with increasing Mach number. Also, the skin friction coefficient magnitudes are higher than the pressure coefficient, demonstrating tangential forces' dominance over the normal forces.

c) Heat transfer coefficient.   The variation of heat transfer coefficient (C_h) for different Ma on the upstream, downstream and the base surface of the cavity is shown in Fig. 13(a–b). C_h is given by

$$C_h = \frac{q_w}{\frac{1}{2}\rho_\infty U_\infty{}^3} \tag{10}$$

where q_w represents the heat flux at the wall, U_∞ is the free-stream velocity and ρ_∞ denotes the free-stream density. The heat flux at the wall is extracted by computing the summation of the net energy flux of impinging molecules on the surface, with the flux being positive towards the surface. It is given by,

$$q_w = q_{inc} - q_{ref}$$

$$= \frac{F_N}{A\Delta t}\left\{ \sum_{j=1}^{N}\left[\frac{1}{2}m_j c_j{}^2 + e_{R_j} + e_{V_j}\right]_{inc} - \sum_{j=1}^{N}\left[\frac{1}{2}m_j c_j{}^2 + e_{R_j} + e_{V_j}\right]_{ref} \right\} \tag{11}$$

where c represents molecular velocity, e_R and e_V represent the rotational and vibrational energies, respectively.

Figure 13(a) shows that the heat transfer coefficient C_h which shows contrasting trends for different Ma. Towards the upstream end, the magnitude of C_h is highest for Ma $= 10$ in comparison with the other cases. Also, the profiles show a gradual decrease for the case of Ma $= 5$, whereas for the other cases the
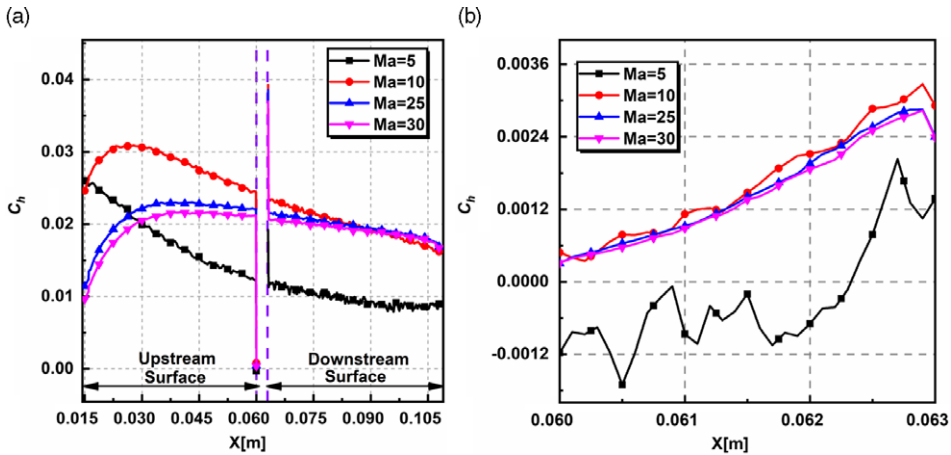
Figure 13. *Variation of heat transfer coefficient C_h (a) on the upstream and downstream surfaces (b) on the cavity base for various* Ma.

C_h gradually increases and shows a decline after that. The differing profiles are possibly caused by the varying boundary layer thickness at the separation [70]. Along the downstream surface the C_h shows a declining trend for different Ma, though, the reduction in C_h is very minimal. Inside the cavity as shown in Fig. 13(b), the heat transfer coefficient C_h is found to be negative for Ma = 5 for a considerable part of the cavity. However, towards the end of the cavity the C_h is found to recover and attain a positive value. For the other cases, the C_h values are fairly similar and are found to increase along the cavity length gradually. At the end of the cavity the C_h values are positive for all the cases due to viscous dissipation, which causes an increase in the wall heat flux and consequently the heat transfer coefficient.

4.2 Influence of Knudsen number

In this section, the influence of the Knudsen number (Kn) is presented. The various Kn considered for analysis were 0.05, 0.10, 1.06, 10.33 and 21.10. The Mach number and wall temperature was fixed to Ma = 25 and $T_w = 4T_\infty$ respectively.

4.2.1 Flow properties

a) Velocity field. The non-dimensional velocity variation for different Kn at sections $X = 30$mm, $X = 59$mm, $X = 61$mm, and $X = 93$mm is shown in Fig. 14(a–d). The non-dimensional velocity is similar in appearance upstream of the cavity at $X = 30$mm and $X = 59$mm. Inside the cavity at $X = 61$mm, the velocity magnitudes are negative due to the recirculation effects. This trend is also observed in the continuum study conducted by Camussi et al. [69]. Also, up to the cavity height, the velocity field is not influenced by the rarefaction effects as they are relatively the same and are found to overlapping. However, the rarefaction affects the velocity field above the cavity height, and the profiles show a deviation. At the exit of the domain at $X = 93$mm, the profiles resemble those observed upstream of the cavity. It is found that there is a substantial velocity slip at the walls at all sections, except inside the cavity where the velocity slip is relatively the same for different Kn. This velocity slip increases with rarefaction and falls in line with the results of Ejtehadi et al. [71].

Along the transverse direction, the non-dimensional velocity reduces with an increase in Kn. As Kn increases, the molecular mean free path increases substantially, resulting in the more significant propagation of the wall effects into the flow domain. This is corroborated quantitively by extracting the boundary layer thickness (δ). Here, the boundary layer thickness (δ) is calculated by considering
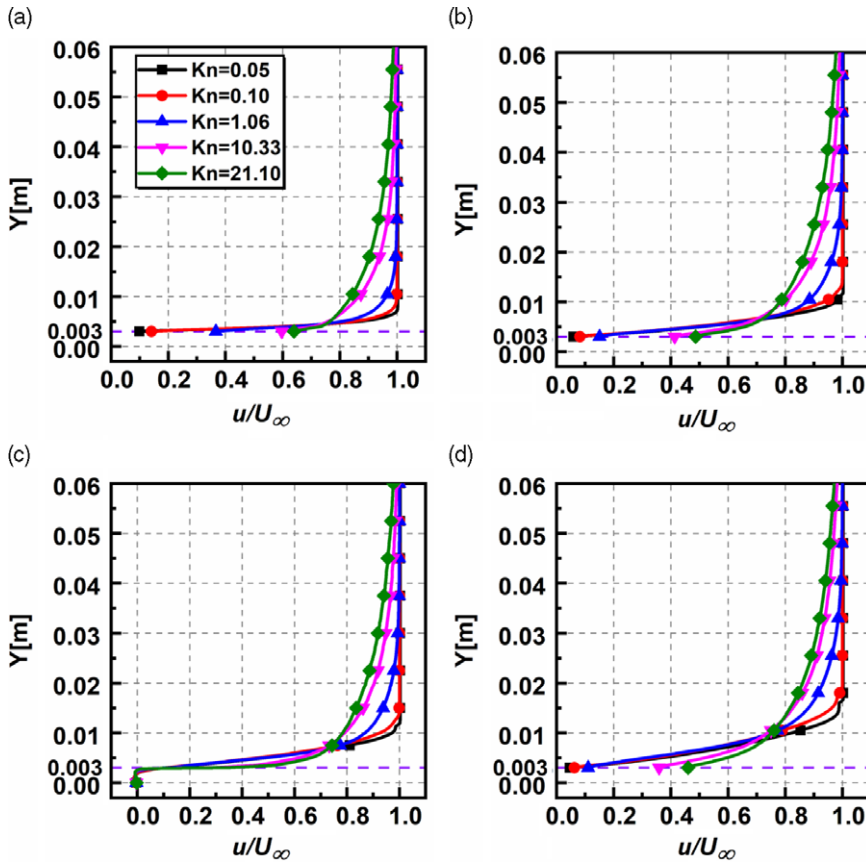
Figure 14. *Non-dimensional velocity variation for various* Kn *at (a)* $X = 30$mm, *(b)* $X = 59$mm, *(c)* $X = 61$mm, *(d)* $X = 93$mm.

$u/U_\infty = 0.99$. For the top surface location considered in the present study, the boundary layer is fully established for different Kn, except $Kn = 21.10$, which shows a developing trend. For a particular location of $X = 59$mm, (δ) and (δ/H) are given in Table 5.

The velocity streamlines for different Kn are depicted in Fig. 15. It is observed that for all Kn, a recirculation region exists. Furthermore, streamlines of the free-molecular flow for the case of $Kn = 10.33, 21.10$ suggest that there exists a secondary smaller recirculation region. The vortex centre shifts towards the top of the cavity as the rarefaction increases. The location of the primary vortex for different Kn is shown in Table 6.

b) Pressure field. The non-dimensional pressure variation for different Kn at sections $X = 30$mm, $X = 59$mm, $X = 61$mm and $X = 93$mm is shown in Fig. 16(a–d). The pressure plots are found to behave in a similar manner in all the sections; however, the magnitudes differ. The near-wall pressure in all the sections is higher than the corresponding free-stream pressure due to the stagnation effects. Also, in the transverse direction, pressure attains free-stream magnitude considerably quicker in the slip regime. Furthermore, the compressibility effects of the flow create a pressure surge just at the level of the cavity height. Inside the cavity at $X = 61$mm, the magnitudes of pressure are the same order as the free-stream. In contrast, above the cavity (for $Y > 0.003$), the magnitudes attain a peak (owing to the presence of shock layer upstream) and gradually decrease and attain a free-stream value. For assessment, at section $X = 61$mm, the peak pressure ratios are 15.36, 18.96, 58.57, 99.08 and 90.73 for Kn 0.05, 0.1, 1.06, 10.33 and 21.10. Downstream of the cavity at $X = 93$mm, the pressure magnitudes are relatively lower.

Table 5. *Boundary layer thickness (δ) for various* Kn *at X = 59mm*

Kn	0.05	0.10	1.06	10.33	21.10
δ(mm)	3.65	4.9	12.25	39.4	–
δ/h	1.21	1.63	4.08	13.13	–
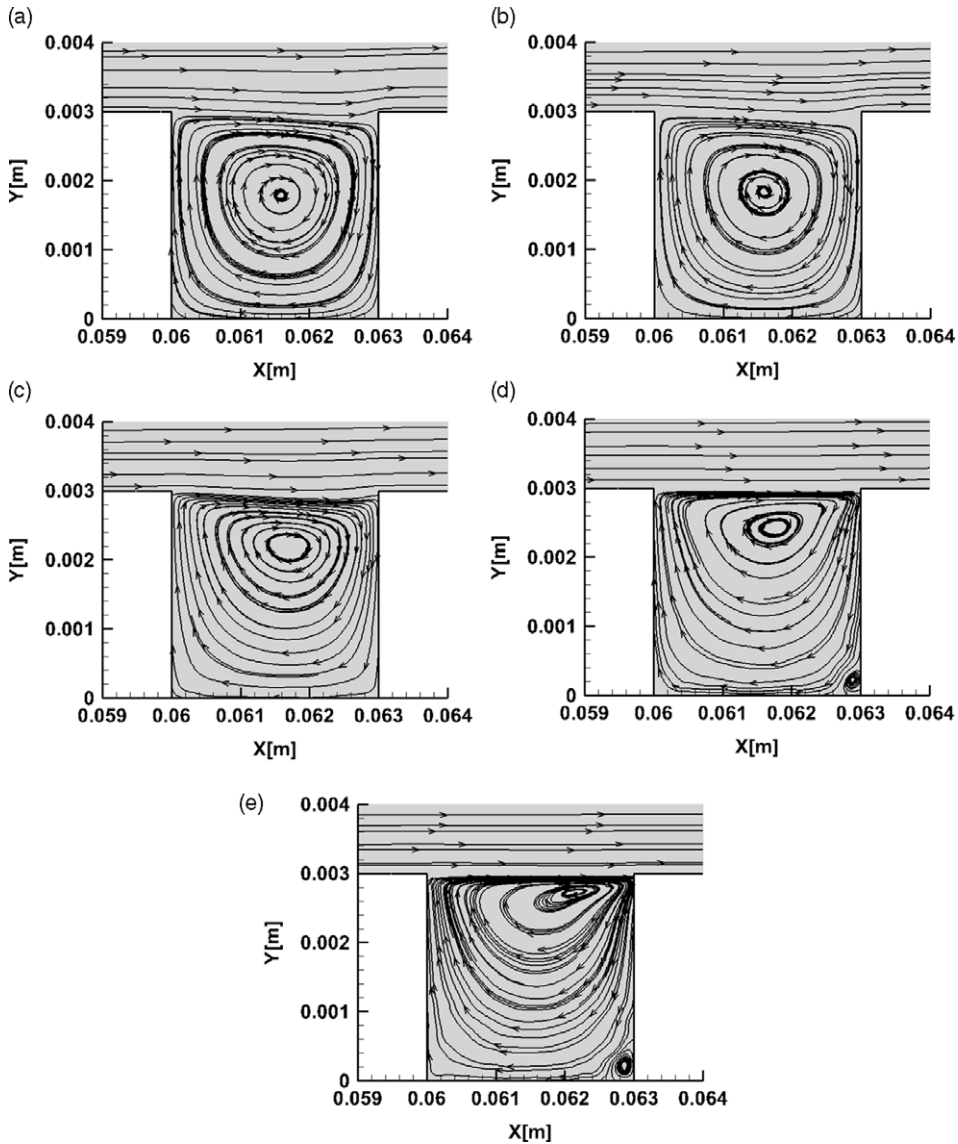
Figure 15. *Streamlines inside the cavity for (a)* Kn = 0.05, *(b)* Kn = 0.1, *(c)* Kn = 1.06, *(d)* Kn = 10.33, *(e)* Kn = 21.10.

c) Temperature field.   The non-dimensional temperature (T/T_∞) variation for various Kn at sections $X = 30$mm, $X = 59$mm, $X = 61$mm, and $X = 93$mm is shown in Fig. 17(a–d). The temperature profiles show a similar trend as the pressure and the magnitudes of temperature increase with increasing Kn. The compressible nature of the incoming flow leads to a significant rise in temperature at the walls.

**Table 6.** *Variation of the centre of the primary vortex for different* Kn

Knudsen number	Primary vortex location
	(X_c, Y_c) [mm]
Kn = 0.05	(1.6,1.8)
Kn = 0.1	(1.7,1.8)
Kn = 1.06	(1.8,2.2)
Kn = 10.33	(1.9,2.5)
Kn = 21.10	(2.3,2.8)
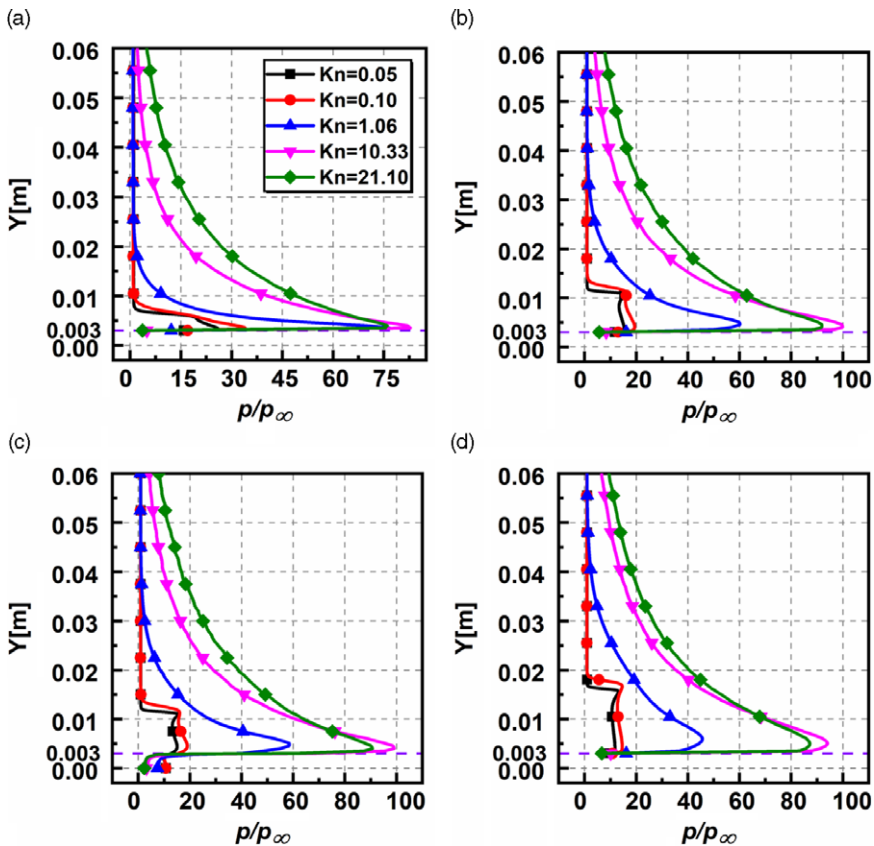
Figure 16. *Non-dimensional pressure variation for various* Kn *at (a)* $X = 30$mm, *(b)* $X = 59$mm, *(c)* $X = 61$mm, *(d)* $X = 93$mm.

However, in contrast, inside the cavity at $X = 61$mm, the near-wall temperature is similar for different Kn and is of the same order as the free-stream temperature.

The non-dimensional temperature surges near the cavity height level and then attains free-stream temperature in the transverse direction. Also, at a given transverse location, it is found that the temperature surges with Kn. The number density of the molecules reduces with rarefaction; thereby, the viscous heating generated in the shear layer is distributed among lesser molecules causing a temperature rise. However, at lower levels of rarefactions where the molecules are significantly higher, the same intensity of viscous heating gets distributed among more molecules, inciting a reduced temperature gain.
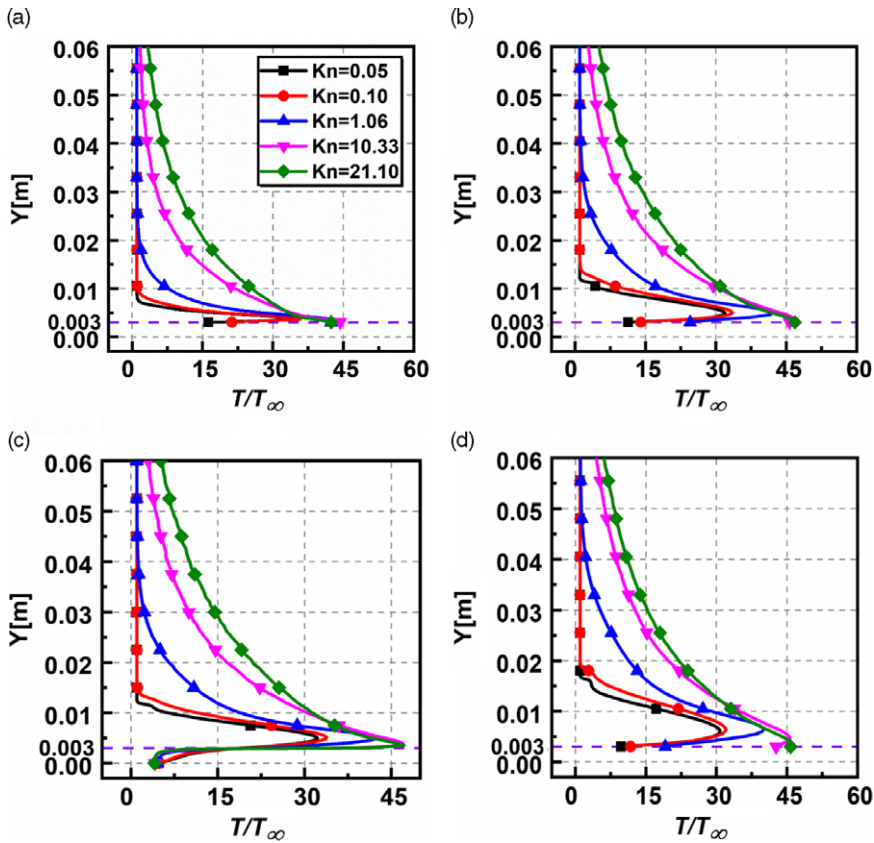
Figure 17. *Non-dimensional temperature variation for various* Kn *(a)* $X = 30$mm, *(b)* $X = 59$mm, *(c)* $X = 61$mm, *(d)* $X = 93$mm.

For quantitative assessment, at the section $X = 61$mm, the non-dimensional temperature at $Y = 0.03$ are 1.00, 0.99, 2.31, 10.02 and 14.53 for Kn 0.05, 0.1, 1.06, 10.33 and 21.10.

4.2.2 Aerodynamic surface properties

a) Pressure coefficient. The variation of pressure coefficient (C_p) for different Kn on the upstream, downstream and the base surface of the cavity is shown in Fig. 18(a–b). The plot shows distinct trends in the slip regime where the profiles are similar for Kn $= 0.05$, 0.10. Also, in the transition and free-molecular regimes, the profiles behave similarly. On the upstream surface, the pressure coefficient C_p in the slip regime, attains a peak at a very short distance from the leading edge and then shows a gradually declining trend towards the edge of the cavity. The early peaks can probably be due to the relatively higher magnitude of near-wall pressure, as seen in Fig. 18(a). In contrast in the transition and free-molecular regime, the C_p gradually rises along the flow direction (X). The peak C_p on the upper surface is observed at X locations of 17.45, 20, 59, 59.40 and 59.45mm for Kn 0.05, 0.1, 1.06, 10.33 and 21.10. Along the downstream surface, the magnitudes of C_p are higher in the beginning and show a reduction towards the outlet for slip regime. For the other regimes, C_p attains a peak and then decreases. Inside the cavity, as shown in Fig. 18(b), the spatial variation in the pressure coefficient C_p is nominal for different Kn and is found to be unaffected by the rarefaction effects.
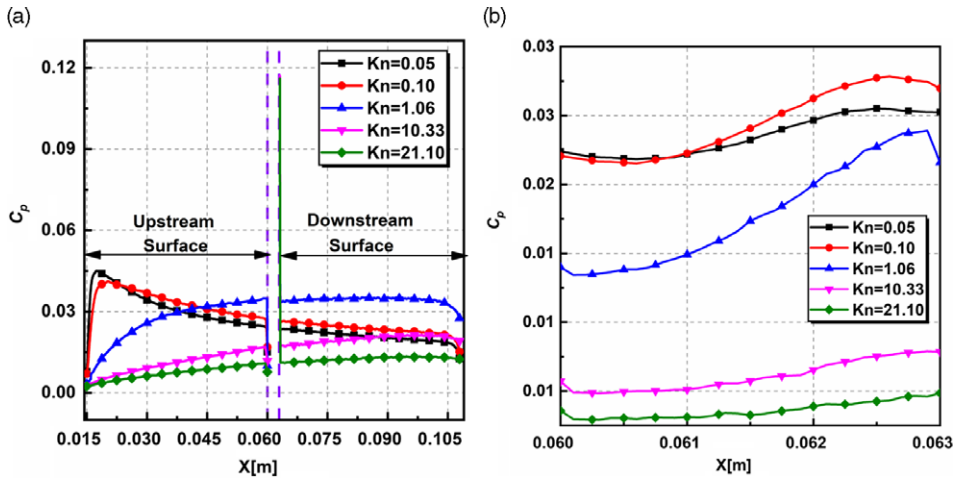
Figure 18. *Variation of pressure coefficient C_p (a) on the upstream and downstream surfaces (b) on the cavity base for various* Kn.
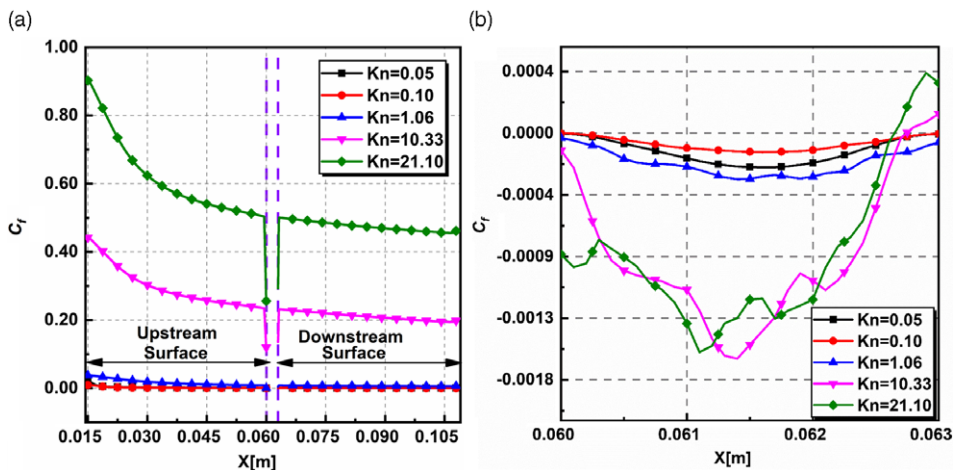

Figure 19. *Variation of skin friction coefficient C_f (a) on the upstream and downstream surfaces (b) on the cavity base for various* Kn.

b) Skin friction coefficient.   The skin friction coefficient (C_f) variation for different *Kn* on the upstream, downstream and the base surface of the cavity is shown in Fig. 19(a–b). The plot shows that the skin friction coefficient C_f at a given location increases with increasing Kn. From Equation (2), as Kn increases, Re diminishes causing the viscous forces to dominate compared to the inertial forces, which leads to an increase in shear stress and C_f. Due to the strong near-wall velocities at the leading edge of the inlet, the C_f is found to attain a peak value. Along the upstream surface, C_f shows a declining trend and attains a lower magnitude at the edge of the cavity. Further, as the flow begins to achieve a high degree of rarefaction, the magnitude of C_f tends to increase significantly. For instance, C_f at the inlet, increases by two folds on transitioning from Kn = 10.33 to Kn = 21.10. Along the downstream surface, the C_f decreases very marginally. Inside the cavity, as shown in Fig. 19(b), the C_f is negative for all the cases due to recirculation observed in the streamline plot (see Fig. 15). The decrease in C_f is higher in the free-molecular regime when compared to the other regimes. Also, in the free-molecular regime, the
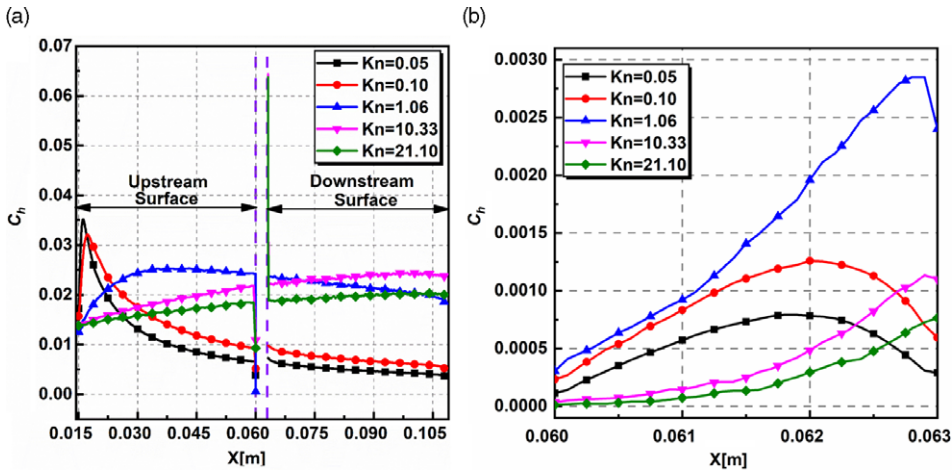
Figure 20. *Variation of heat transfer coefficient C_h (a) on the upstream and downstream surfaces (b) on the cavity base for various* Kn.

variation in C_f is significant due to the asymmetry of the vortex formed, whereas for Kn ≤ 1.06, the C_f is relatively constant due to the symmetry in the vortex.

c) Heat transfer coefficient. The variation of heat transfer coefficient (C_h) for different Kn on the upstream, downstream and the base surface of the cavity is shown in Fig. 20(a–b). The plots of C_h and C_p are similar in appearance. Also, on the upper surface, the profiles are dissimilar for different Kn. Along the upper surface of the cavity, near the leading edge, the heat transfer coefficient C_h show a sudden peak in the slip regime, whereas in the other regimes the C_h shows a gradually increasing trend. Near cavity base, flow expansion caused the temperature reducing, leading to a drop in the heat transfer coefficient C_h. Along the lower surface the C_h values are relatively constant in the slip regime, whereas they show a gradual increase in other regimes. As the rarefaction increases, particles from the middle of the computational domain collide due to the increased mean free path, causing a rise in the heat transfer coefficient.

4.3 Comparison with chemically reacting flows

The present study involves hypersonic flow conditions, resulting in an energised system where the gas's vibrational modes are triggered, and chemical reactions take place. Consequently, the influence of these vibrational excitations on the flow properties needs to be studied.

Over the years, several chemical reaction models for DSMC have been developed. Bird [59] introduced the Total Collision Energy (TCE) model. It is one such popular chemical reaction model that uses the equilibrium kinetic theory to translate the Arrhenius rate coefficients into collision probabilities. Alternatively, Bird [72] proposed the Quantum-Kinetic (Q-K) chemistry model, a molecular-level chemistry model that employs the fundamental molecular properties instead of the classical TCE model, which relies on the availability of experimental data. The current research utilises the Q-K chemistry model to simulate chemical reactions of five species of air with 19 chemical reactions. This study is carried out using *dsmcFoam+*. Two chemical reaction types are relevant to the present discussion Dissociation (No. 1–15 in Table 7) and Exchange reactions (No. 16–19 in Table 7).

To define the overall temperature, the weighted average of translational, rotational and vibrational temperatures [73] is taken and is given by,

$$T_{ov} = \frac{3T_T + \xi_R T_R + \xi_V T_V}{3 + \xi_R + \xi_V} \tag{12}$$

Table 7. *List of chemical reactions employed*

No.	Reaction	Heat of formation J $\times 10^{19}$
1.	$O_2 + N \rightarrow O + O + N$	8.197
2.	$O_2 + NO \rightarrow O + O + NO$	8.197
3.	$O_2 + N2 \rightarrow O + O + N_2$	8.197
4.	$O_2 + O_2 \rightarrow O + O + O_2$	8.197
5.	$O_2 + O \rightarrow O + O + O$	8.197
6.	$N_2 + O \rightarrow N + N + O$	15.67
7.	$N_2 + O_2 \rightarrow N + N + O_2$	15.67
8.	$N_2 + NO \rightarrow N + N + NO$	15.67
9.	$N_2 + N_2 \rightarrow N + N + N_2$	15.67
10.	$N_2 + N \rightarrow N + N + N$	15.67
11.	$NO + N_2 \rightarrow N + O + N_2$	10.43
12.	$NO + O_2 \rightarrow N + O + O_2$	10.43
13.	$NO + NO \rightarrow N + O + NO$	10.43
14.	$NO + O \rightarrow N + O + O$	10.43
15.	$NO + N \rightarrow N + O + N$	10.43
16.	$NO + O \rightarrow O_2 + N$	2.719
17.	$N_2 + O \rightarrow NO + N$	5.175
18.	$O_2 + N \rightarrow NO + O$	−2.719
19.	$NO + N \rightarrow N_2 + O$	−5.175

where ξ represents the degree of freedom, and the subscripts T, R and V stand for translation, rotation and vibration, respectively.

The following equations give the translational, rotational and vibrational temperatures,

$$T_T = \frac{1}{3k_b} \frac{\sum_{j=1}^{N} m_j c'^2}{N} \tag{13}$$

$$T_R = \frac{2}{k_b \xi_R} \frac{\sum_{j=1}^{N} (\varepsilon_R)_j}{N} \tag{14}$$

$$T_V = \frac{\Theta_V}{\ln\left(1 + \frac{k_b \Theta_V}{\sum_{j=1}^{N} (\varepsilon_V)_j}\right)} \tag{15}$$

where ε_R and ε_V represent the average rotational and vibrational energies, respectively, k_b is the Boltzmann constant, and Θ_V denotes the characteristic vibrational temperature, having a value equal to 3371 and 2256K for N_2 and O_2 respectively. The rotational and vibrational collision relaxation number considered in the study was 5 and 50, respectively.

To compare chemically reacting and non-reacting cases, the flow over cavity at Ma = 25 was studied for different Kn. When chemical reactions were considered and compared against the non-reacting flows, the flow-field properties such as velocity, pressure and density showed no marked difference. Hence, the discussion will be limited to only the temperature field. Figure 21 shows the non-dimensional temperature contours for different components of the temperature Kn = 1.06.

The vibrational component of the temperature in Fig. 21(a) is relatively lower in magnitude than the other components. The vibrational excitations appear not to affect the cavity, and as a result, the vibrational temperature shows no marked difference. However, a temperature surge is observed towards the outlet. The rotational component of the temperature is shown in Fig. 21(b). Its order of magnitude is the same as that of the vibrational component with only marginally higher values. Figure 21(c) and (d),
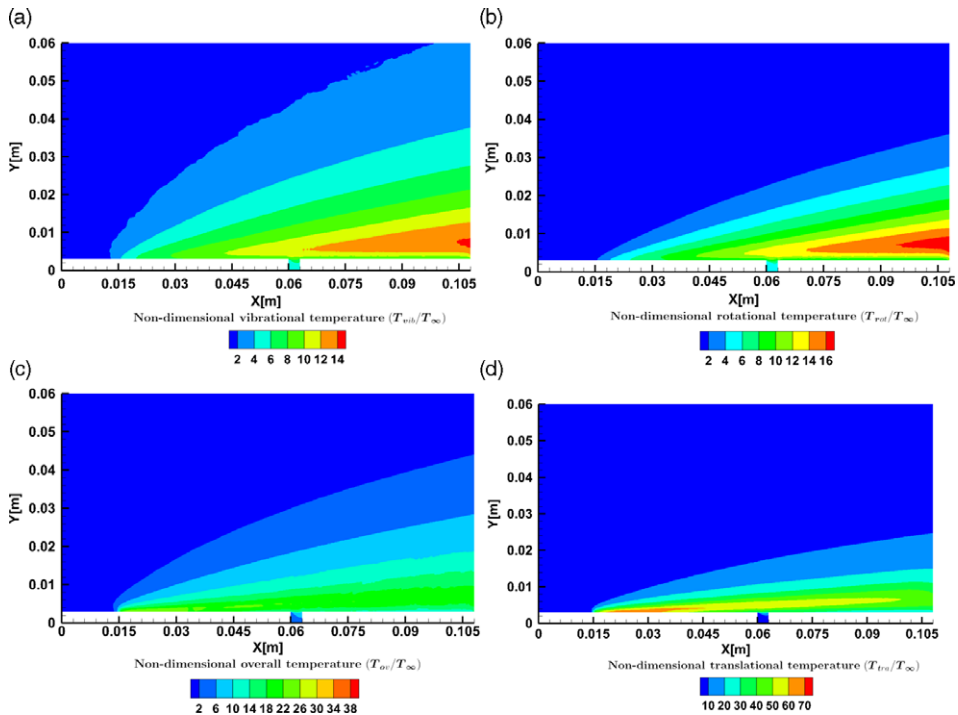
Figure 21. *Contours of non-dimensional (a) vibrational, (b) rotational, (c) overall, and (d) translational temperature for* Ma $= 25$ *and* Kn $= 1.06$.

the overall and translational components, respectively. Near the wall, the translational temperature has a much larger magnitude, which can be credited to the viscous heating effects observed in the shear layer at the top of the cavity and near the wall. The rotational and vibrational temperatures show similar behaviour. This entire effect is reflected in the contours of the overall temperature in Fig. 21(c). Rapid flow expansion is observed just upstream of the cavity and results in expansion cooling inside the cavity. This expansion cooling is the reason for the lower magnitudes of the translational temperature inside the cavity. Expansion cooling also affects the translational temperature downstream near the outlet, resulting in lower translational temperature values. At the outlet, there is a considerable decrease in the magnitude of the translational temperature. Contrasting to this behaviour, an increase in the rotational and vibrational temperatures near the outlet is visible, as shown in Fig. 21(a) and (b), respectively, due to the non-equilibrium effects. Figure 21(c) shows that the cumulative consequence of enhanced rotational and vibrational temperature is compensated by the decreased translational temperature downstream of the cavity. As a result, a relatively uniform overall temperature variation is observed downstream of the cavity.

The non-dimensional temperature variation for different Kn at sections $X = 30$mm, $X = 59$mm, $X = 61$mm and $X = 93$mm is shown in Fig. 22(a–d). It is observed that both chemically reacting and non-reacting flows follow similar trends for different Kn. However, a considerable difference in the predicted value is observed for the chemically reacting flows. The highest temperature in the shear layer is computed, and the relative change is evaluated with respect to the non-reacting flow for various locations. For instance, at $X = 30$ mm the maximum temperature ratio values predicted by non-reacting flow, vary with chemically reacting flow by roughly 66.52%, 80.12%, 49.78%, 6.76% and 0.79% for Kn $= 0.05$, 0.10, 1.06, 10.33 and 21.10. Similarly, inside the cavity at $X = 61$mm, the change in the maximum temperature is more than 35% for all Kn.
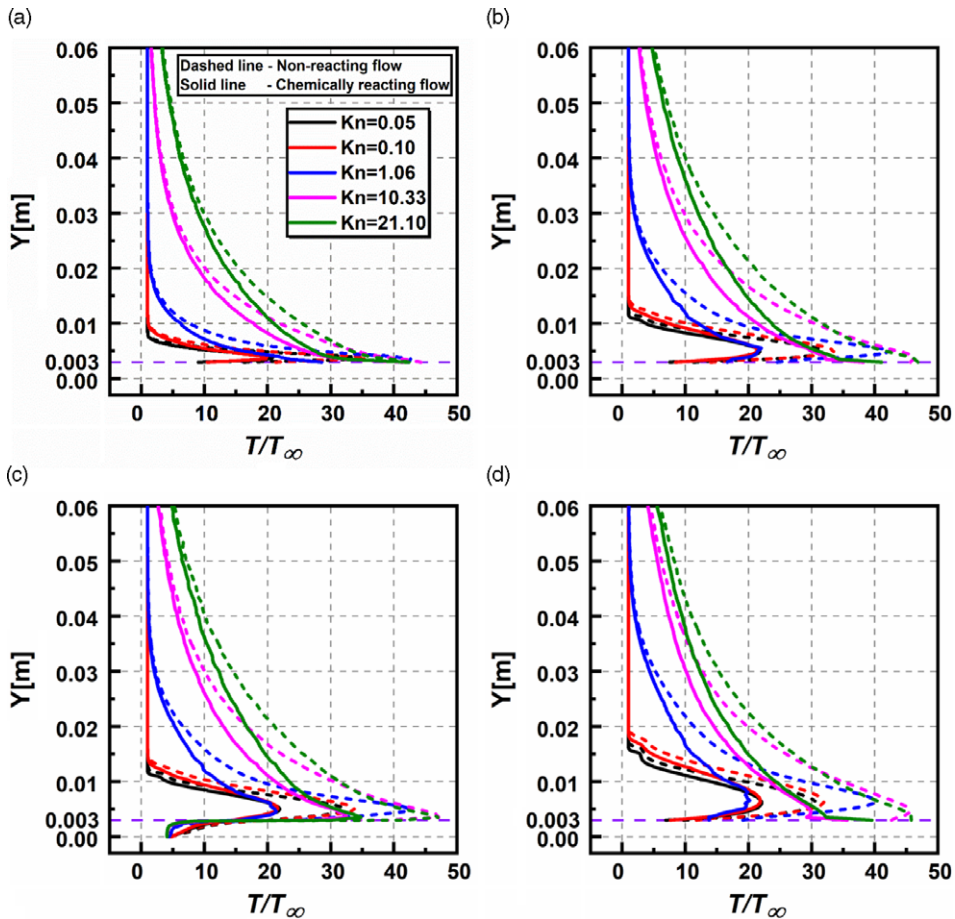
Figure 22. *Non-dimensional temperature variation for various* Kn *(a) X = 30mm, (b) X = 59mm, (c) X = 61mm, (d) X = 93mm for reacting and non-reacting cases.*

5.0 Conclusion

The flow over the cavity can be approximated as one of the abnormalities that can occur on the surface of a hypersonic vehicle, the study of which aids in the understanding of the flow dynamics over such vehicles. This study explores the influence of Ma and Kn on the flow field and surface properties. The DSMC method is used as a numerical tool to conduct the studies. The numerical model is validated with the literature results, and a good agreement is found among them. The main conclusions are listed as follows:

1. The flow field properties such as velocity, pressure and temperature significantly rise with Mach number, owing predominantly to the viscous dissipation. Inside the cavity, the trends were similar except for the velocity field that showed a contrasting trend.

2. Rarefaction of the flow caused a reduction in the velocity due to the increased boundary layer thickness. The pressure field and temperature field increased with increasing Knudsen number. Inside the cavity, no definitive trend was observed.

3. The presence of the cavity is felt by the flow field only in the immediate vicinity of it, and trends in the variation of the flow properties far away from it are mostly unaffected.

4. Inside the cavity, flow recirculation was observed in all regimes. The recirculation was symmetric in the slip regime and asymmetric in other regimes. Secondary vortices set in for the free-molecular flows.

5. Magnitude of the aerodynamic coefficients (i) decrease with Ma, both inside the cavity and on its upstream and downstream surfaces (ii) show more complex trends with an increase in Kn both inside and outside the cavity. They increase in the slip regime and decrease in the transitional and free-molecular regimes, whereas only C_f shows an opposing variation.

6. The flow-field properties such as velocity, pressure and density showed no marked difference when compared against the non-reacting flows. In contrast, considerable difference was observed in the temperature field as the chemical reactions result in absorption of the energy by the fluid. The temperature differences were substantial, particularly in the shear layer.

This study presents a detailed analysis of the hypersonic flow over a cavity and offers valuable insights into the physics of individual flow and aerodynamic properties for the cases considered.

References

[1] Kumar, S. and Vengadesan, S. The effect of fin oscillation in heat transfer enhancement in separated flow over a backward facing step, *Int. J. Heat Mass Transfer*, 2019, **128**, pp 954–963. https://doi.org/10.1016/j.ijheatmasstransfer.2018.09.001.

[2] Morgan, K., Periaux, J. and Thomasset, F. *Analysis of Laminar Flow Over a Backward Facing Step*, Springer, 1984.

[3] Chen, L., Asai, K., Nonomura, T., Xi, G. and Liu, T. A review of backward-facing step (BFS) flow mechanisms, heat transfer and control, *Ther. Sci. Eng. Progress.*, 2018, **6**, pp 194–216.

[4] Stüer, H., Gyr, A. and Kinzelbach, W. Laminar separation on a forward facing step, *Eur. J. Mech. B/Fluids*, 1999, **18**, pp 675–692. https://doi.org/10.1016/S0997-7546(99)00104-1.

[5] Zukoski, E.E. Turbulent boundary-layer separation in front of a forward-facing step, *AIAA J.*, 1967, **5**, pp 1746–1753. https://doi.org/10.2514/3.4299.

[6] Gallis, M.A., Boyles, K.A. and LeBeau, G.J. DSMC Simulations in Support of the STS-107 Accident Investigation, in *AIP Conference Proceedings*, American Institute of Physics, 2005, pp 1211–1216.

[7] Board, C.A.I. *Report of Columbia Accident Investigation Board*, vol. I, NASA, January, 2006.

[8] Bird, G. Sophisticated DSMC short course, in *Direct Simulation Monte Carlo Theory, Methods & Applications Conference*, Hosted by Sandia National Laboratory, 2007.

[9] Bird, G., Gallis, M., Torczynski, J. and Rader, D. Accuracy and efficiency of the sophisticated direct simulation Monte Carlo algorithm for simulating noncontinuum gas flows, *Phys. Fluids (1994)*, 2009, **21**, p 017103.

[10] He, X., He, B. and Cai, G. Simulation of rocket plume and lunar dust using DSMC method, *Acta Astronaut.*, 2012, **70**, pp 100–111. https://doi.org/10.1016/j.actaastro.2011.07.014.

[11] Jun, E. and Boyd, I.D. Assessment of the LD-DSMC hybrid method for hypersonic rarefied flow, *Comput. Fluids*, 2018, **166**, pp 123–138. https://doi.org/10.1016/j.compfluid.2018.02.005.

[12] Darbandi, M. and Roohi, E. A hybrid DSMC/Navier-Stokes frame to solve mixed rarefied/nonrarefied hypersonic flows over nano-plate and micro-cylinder: HYBRID DSMC/NS FRAME TO SOLVE RAREFIED/NON-RAREFIED MICRO/NANOFLOWS, *Int. J. Numer. Methods Fluids*, 2013, **72**, pp 937–966. https://doi.org/10.1002/fld.3769.

[13] Mohammadzadeh, A., Roohi, E., Niazmand, H., Stefanov, S. and Myong, R.S. Thermal and second-law analysis of a micro- or nanocavity using direct-simulation Monte Carlo, *Phys. Rev. E Stat. Nonlin. Soft. Matter Phys.*, 2012, **85**, p 056310. https://doi.org/10.1103/PhysRevE.85.056310.

[14] Zheng, P., Wu, J., Biqi, W. and Zhang, Y. Design and numerical investigation on the intake of atmosphere-breathing electric propulsion, *Acta Astronaut.*, 2021, **188**, pp 215–228. https://doi.org/10.1016/j.actaastro.2021.07.036.

[15] Loth, E., Tyler Daspit, J., Jeong, M., Nagata, T. and Nonomura, T. Supersonic and hypersonic drag coefficients for a sphere, *AIAA J.*, 2021, pp 3261–3274. https://doi.org/10.2514/1.J060153.

[16] Li, S. and Xiao, H. A unified theory for modelling nonequilibrium and equilibrium gas flows, *Acta Astronaut.*, 2021, **182**, pp 486–497. https://doi.org/10.1016/j.actaastro.2021.02.038.

[17] Charwat, A.F., Roos, J.N., Dewey, F.C. and Hitz, J.A. An investigation of separated flows - Part I: The pressure field, *J. Aerosp. Sci.*, 1961, **28**, pp 457–470. https://doi.org/10.2514/8.9037.

[18] Charwat, A.F., Dewey, C.F., Roos, J.N. and Hitz, J.A. An investigation of separated flows-part II: Flow in the cavity and heat transfer, *J. Aerosp. Sci.*, 1961, **28**, pp 513–527. https://doi.org/10.2514/8.9099.

[19] Bertram, M.H. and Wiggs, M.M. Effect of surface distortions on the heat transfer to a wing at hypersonic speeds, *AIAA J.*, 1963, **1**, pp 1313–1319. https://doi.org/10.2514/3.1786.

[20] Nestler, D.E. and Saydah, A.R. Heat transfer to steps and cavities in hypersonic turbulent flow, *AIAA J.*, 1969, **7**, pp 1368–1370. https://doi.org/10.2514/3.5351.

[21] Charwat, A.F. Separation of a supersonic accelerated flow over notches, *AIAA J.*, 1971, **9**, pp 1656–1657. https://doi.org/10.2514/3.6413.

[22] Nestler, D.E. An experimental study of hypersonic cavity flow, *J. Spacecr. Rockets,* 1982, **19**, pp 195–196.

[23] Mankodi, T.K., Bhandarkar, U.V. and Puranik, B.P. Hypersonic flow over Stardust Re-entry Capsule using ab-initio based chemical reaction model, *Acta Astronaut.*, 2019, **162**, pp 243–255. https://doi.org/10.1016/j.actaastro.2019.06.021.

[24] Akhlaghi, H., Roohi, E. and Stefanov, S. Ballistic and collisional flow contributions to anti-Fourier heat transfer in rarefied cavity flow, *Sci. Rep.*, 2018, **8**, pp 1–13.

[25] Roohi, E., Shahabi, V. and Bagherzadeh, A. On the vortical characteristics and cold-to-hot transfer of rarefied gas flow in a lid driven isosceles orthogonal triangular cavity with isothermal walls, *Int. J. Therm. Sci.*, 2018, **125**, pp 381–394. https://doi.org/10.1016/j.ijthermalsci.2017.12.005.

[26] Mohammadzadeh, A., Roohi, E. and Niazmand, H. A parallel DSMC investigation of monatomic/diatomic gas flows in a micro/nano cavity, *Numerical Heat Transf A: Appl.*, 2013, **63**, pp 305–325. https://doi.org/10.1080/10407782.2013.730463.

[27] Creighton, S. and Hillier, R. Experimental and computational study of unsteady hypersonic cavity flows, *Aeronaut. J.*, 2007, **111**, pp 673–688.

[28] Morgenstern, A. and Chokani, N. Hypersonic flow past open cavities, *AIAA J.*, 1994, **32**, pp 2387–2393.

[29] Palharini, R.C., Scanlon, T.J. and Reese, J.M. Aerothermodynamic comparison of two- and three-dimensional rarefied hypersonic cavity flows, *J. Spacecr. Rockets*, 2014, **51**, pp 1619–1630. https://doi.org/10.2514/1.A32746.

[30] Paolicchi, L.T.L.C. and Santos, W.F.N. Length-to-depth ratio effects on aerodynamic surface quantities of a hypersonic gap flow, *AIAA J.*, 2018, **56**, pp 780–792. https://doi.org/10.2514/1.J055826.

[31] Guo, G. and Luo, Q. Flowfield structure characteristics of the hypersonic flow over a cavity: From the continuum to the transition flow regimes, *Acta Astronaut.*, 2019, **161**, pp 87–100.

[32] Guo, G. and Luo, Q., DSMC investigation on flow characteristics of rarefied hypersonic flow over a cavity with different geometric shapes, *Int. J. Mech. Sci.*, 2018, **148**, pp 496–509. https://doi.org/10.1016/j.ijmecsci.2018.09.022.

[33] Palharini, R.C., Scanlon, T.J. and White, C. Chemically reacting hypersonic flows over 3D cavities: Flowfield structure characterisation, *Comput. Fluids*, 2018, **165**, pp 173–187. https://doi.org/10.1016/j.compfluid.2018.01.029.

[34] Palharini, R.C. and Santos, W.F. The impact of the length-to-depth ratio on aerodynamic surface quantities of a rarefied hypersonic cavity flow, *Aerosp. Sci. Technol.*, 2019, **88**, pp 110–125.

[35] Jin, X., Wang, B., Cheng, X., Wang, Q. and Huang, F. The effects of Maxwellian accommodation coefficient and free-stream Knudsen number on rarefied hypersonic cavity flows, *Aerosp. Sci. Technol.*, 2020, **97**, p 105577. https://doi.org/10.1016/j.ast.2019.105577.

[36] Bird, G.A. *Molecular Gas Dynamics and the Direct Simulation of Gas Flows*, Oxford University Press, New York, 1994.

[37] Jin, X., Huang, F., Cheng, X., Wang, Q. and Wang, B. Monte Carlo simulation for aerodynamic coefficients of satellites in Low-Earth Orbit, *Acta Astronaut.*, 2019, **160**, pp 222–229. https://doi.org/10.1016/j.actaastro.2019.04.012.

[38] Cai, G., Zheng, H., Liu, L., Ren, X. and He, B. Three-dimensional particle simulation of ion thruster plume impingement, *Acta Astronaut.*, 2018, **151**, pp 645–654. https://doi.org/10.1016/j.actaastro.2018.07.007.

[39] Shang, S., Xiang, S., Jiang, L., Wang, W., He, B. and Weng, H. Sputtering distribution of LIPS200 ion thruster plume, *Acta Astronaut.*, 2019, **160**, pp 7–14. https://doi.org/10.1016/j.actaastro.2019.04.008.

[40] You, J., Zhang, X., Zhang, H., Li, C., Xu, Y., Yan, Q., Yu, H., Liu, J., Li, Y., Wang, Y., Zhao, C., Zhang, H., Xu, Y., Chen, L., Lin, H., Fu, Q., Gao, Y., Wang, Y., Wang, W. and Zhi, Q. Analysis of plume–lunar surface interaction and soil erosion during the Chang'E-4 landing process, *Acta Astronaut.*, 2021, **185**, pp 337–351. https://doi.org/10.1016/j.actaastro.2021.05.009.

[41] Walsh, J., Berthoud, L. and Allen, C. Drag reduction through shape optimisation for satellites in Very Low Earth Orbit, *Acta Astronaut.*, 2021, **179**, pp 105–121. https://doi.org/10.1016/j.actaastro.2020.09.018.

[42] Zhang, B., Liu, H. and Jin, S. An asymptotic preserving Monte Carlo method for the multispecies Boltzmann equation, *J. Comput. Phys.*, 2016, **305**, pp 575–588.

[43] Cercignani, C., The Boltzmann equation, In *The Boltzmann Equation and Its Applications*, Springer, 1988, pp 40–103.

[44] Alexander, F.J., Garcia, A.L. and Alder, B.J. Cell size dependence of transport coefficients in stochastic particle algorithms, *Phys Fluids (1994)*, 1998, **10**, pp 1540–1542. https://doi.org/10.1063/1.869674.

[45] Hadjiconstantinou, N.G. Analysis of discretization in the direct simulation Monte Carlo, *Phys Fluids (1994)*, 2000, **12**, pp 2634–2638. https://doi.org/10.1063/1.1289393.

[46] Roohi, E. and Stefanov, S. Collision partner selection schemes in DSMC: From micro/nano flows to hypersonic flows, *Phys. Rep.*, 2016, **656**, pp 1–38. https://doi.org/10.1016/j.physrep.2016.08.002.

[47] Roohi, E., Stefanov, S., Shoja-Sani, A. and Ejraei, H. A generalized form of the Bernoulli Trial collision scheme in DSMC: Derivation and evaluation, *J. Comput. Phys.*, 2018, **354**, pp 476–492. https://doi.org/10.1016/j.jcp.2017.10.033.

[48] Abe, T. Generalized scheme of the no-time-counter scheme for the DSMC in rarefied gas flow analysis, *Comput. Fluids*, 1993, **22**, pp 253–257. https://doi.org/10.1016/0045-7930(93)90057-G.

[49] Prasanth, P. and Kakkassery, J.K. Molecular models for simulation of rarefied gas flows using direct simulation Monte Carlo method, *Fluid Dyn. Res.*, 2008, **40**, p 233.

[50] Scanlon, T.J., Roohi, E., White, C., Darbandi, M. and Reese, J.M. An open source, parallel DSMC code for rarefied gas flows in arbitrary geometries, *Comput. Fluids*, 2010, **39**, pp 2078–2089. https://doi.org/10.1016/j.compfluid.2010.07.014.

[51] White, C., Borg, M.K., Scanlon, T.J., Longshaw, S.M., John, B., Emerson, D.R. and Reese, J.M. dsmcFoam+: An OpenFOAM based direct simulation Monte Carlo solver, *Comput. Phys. Commun.*, 2018, **224**, pp 22–43. https://doi.org/10.1016/j.cpc.2017.09.030.

[52] Akhlaghi, H., Balaj, M. and Roohi, E. Direct simulation Monte Carlo investigation of mixed supersonic–subsonic flow through micro-/nano-scale channels, *Phys. Scr.*, 2013, **88**, p 015401.

[53] Guo, K. and Liaw, G. A review-boundary conditions for the DSMC method, In *35th AIAA Thermophysics Conference*, 2001, p 2953.

[54] U.S. Atmosphere, *US standard atmosphere*, National Oceanic and Atmospheric Administration, 1976.

[55] Leite, P.H.M. and Santos, W.F.N., Computational analysis of the flow field structure of a non-reacting hypersonic flow over forward-facing steps, *J. Fluid Mech.* **763** (2015)pp 460–499. https://doi.org/10.1017/jfm.2014.677.

[56] Nabapure, D., Sanwal, J., Rajesh, S. and Murthy, K.R.C., Investigation of Subsonic and Hypersonic Rarefied Gas Flow over a Backward Facing Step, In *Journal of Physics: Conference Series*, IOP Publishing, 2019, p 012007.

[57] Nabapure, D. and Murthy, K.R.C., DSMC investigation of rarefied gas flow over a 2D forward-facing step: Effect of Knudsen number, *Acta Astronaut.* **178** (2021) pp 89–109. https://doi.org/10.1016/j.actaastro.2020.08.030.

[58] Nabapure, D. and Murthy, K.R.C. Simulation of flow in single and double-sided lid driven square cavities by direct simulation Monte Carlo method, *Ther. Sci.*, 2020, **24**, pp 3031–3045. https://doi.org/10.2298/TSCI180906066N.

[59] Nabapure, D. and Murthy, K.R.C. DSMC simulation of rarefied gas flow over a forward-facing step, In *ICTEA: International Conference on Thermal Engineering*, 2019.

[60] Nabapure, D. and Murthy, K.R.C. Investigation of rarefied open cavity flows in all rarefaction regimes using DSMC method, In *APS Division of Fluid Dynamics Meeting Abstracts*, 2020, pp K18-005.

[61] Nabapure, D., et al. DSMC investigation of rarefied gas flow in a four-sided lid driven cavity: Effect of rarefaction and lid velocities, *J. Computat. Sci.*, 2021, **49**, p 101276.

[62] Nabapure, D., Singh, A. and Murthy, K.R.C. Effect of Mach Number on the Rarefied Gas Flow Over a Forward-Facing Step, Theoretical, Computational, and Experimental Solutions to Thermo-Fluid Systems: Select Proceedings of ICITFES 2020. (n.d.) 451.

[63] Nabapure, D. and Murthy, R.C. DSMC simulation of rarefied gas flow over a wall mounted cube, In *Fluids Engineering Division Summer Meeting*, American Society of Mechanical Engineers, 2019, p V002T02A071.

[64] Nabapure, D. and Murthy, K.R.C. DSMC simulation of rarefied gas flow over a forward-facing step: Effect of expansion ratio, In *AIP Conference Proceedings*, AIP Publishing LLC, 2021, p 030032.

[65] Nabapure, D., Singh, A. and Murthy, K.R.C. Investigation of rarefied flow over backward-facing step in different rarefaction regimes using direct simulation Monte Carlo, *Aeronaut. J.*, 2021, pp 1–28. https://doi.org/10.1017/aer.2021.88.

[66] Nabapure, D. and Murthy, K.R.C. DSMC simulation of rarefied gas flow over a 2D backward-facing step in the transitional flow regime: Effect of Mach number and wall temperature, *Proc. Inst. Mech. Eng. G J. Aerosp. Eng.*, 2020, p 0954410020959872.

[67] Scanlon, T.J., White, C., Borg, M.K., Palharini, R.C., Farbar, E., Boyd, I.D., Reese, J.M. and Brown, R.E., Open-source direct simulation monte carlo chemistry modeling for hypersonic flows, *AIAA J.*, 2015, **53**, pp 1670–1680.

[68] Grotowsky, I.M.G. and Ballmann, J. Numerical investigation of hypersonic step-flows, *Shock Waves*, 2000, **10**, pp 57–72. https://doi.org/10.1007/s001930050179.

[69] Camussi, R., Felli, M., Pereira, F., Aloisio, G., Di Marco, A., Statistical properties of wall pressure fluctuations over a forward-facing step, *Phys Fluids (1994)* **20** (2008) 075113. https://doi.org/10.1063/1.2959172.

[70] Rom, J. and Seginer, A. Laminar heat transfer to a two-dimensional backward facing step from the high-enthalpy supersonic flow in the shock tube, *AIAA J.*, 1964, **2**, pp 251–255. https://doi.org/10.2514/3.2295.

[71] Ejtehadi, O., Roohi, E. and Esfahani, J.A. Detailed investigation of hydrodynamics and thermal behavior of nano/micro shear driven ow using DSMC, *Sci. Iran.*, 2013, p **13**.

[72] Bird, G.A. The Q-K model for gas-phase chemical reaction rates, *Phys Fluids (1994)*, 2011. https://doi.org/10.1063/1.3650424.

[73] Bird, G. *Molecular Gas Dynamics and the Direct Simulation Monte Carlo of Gas Flows*, vol. 508. Clarendon, Oxford, 1994, p 128.